

UNIVERSITA' DEGLI STUDI DI PAVIA



FACOLTA' DI INGEGNERIA

Dottorato di Ricerca in Microelettronica

Ciclo XXIII

**SOLAR CELLS MODELLIZATION AND POWER
MANAGEMENT IN PHOTOVOLTAIC GENERATION SYSTEMS**

Tutor:

Chiar.mo Prof. Enrico DALLAGO

Coordinatore del Corso di Dottorato:

Chiar.mo Prof. Franco MALOBERTI

Tesi di Dottorato di:

Patrick MERHEJ

To my father...

CONTENTS

Introduction	1
Solar cells models.....	3
1.1 Introduction	3
1.2 Methods of description for parameters evaluation.....	8
1.2.1 Newton-Raphson method (N-R)	9
1.2.2 Single variable optimization method (SVO).....	12
1.2.3 Capacitance estimation	14
1.3 Experimental setup.....	16
1.3.1 Newton-Raphson.....	16
1.3.2 Single variable optimization	16
1.4 Methods validation.	17
1.4.1 Newton-Raphson.....	17
1.4.2 Single variable optimization	20
1.4.3 Capacitance estimation	20
1.5 Methods application	22
1.5.1 Newton-Raphson.....	22
1.5.2 Single variable optimization	24
1.5.3 Dynamic model	26
1.6 Environmental model.....	28
1.6.1 Parameters dependence on G and T	28
1.7 Mismatch.....	31
1.7.1 Shadow effect	31
1.7.2 Temperature effects.....	37

1.7.3	Considerations	38
1.8	Conclusion	39
Maximum Power Point Trackers		40
2.1	Introduction	40
2.2	Converter topologies for MPPT	43
2.2.2	Theoretic analysis	45
2.3	MPPT	47
2.3.1	The indirect methods	47
2.3.1.1	Curve-fitting	47
2.3.1.2	Look-up table method	48
2.3.1.2	Open-circuit voltage	48
2.3.1.3	Short-circuit current	49
2.3.1.4	Model parameters	49
2.3.2	The direct methods	50
2.3.2.1	Perturb and Observe	50
2.3.2.2	Incremental conductance method	53
2.3.2.3	The only voltage photovoltaic method	54
2.4	Capacitance load	56
2.4.1	Dynamic response	56
2.5	Bridge capacitor	59
2.5.1	MPP detection	59
2.5.2	Simulation results	62
2.5.3	Experimental results and considerations	64
2.6	Conclusion	66
Conclusion		67
Bibliography		69

INTRODUCTION

A photovoltaic (PV) power system converts solar energy into another useful energy form. Basically, this system is a combination of four components as can be seen in Fig. 1.

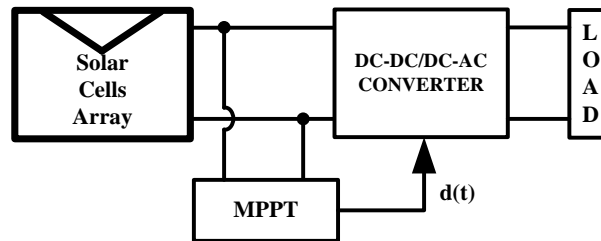


Fig. 1 Block diagram of a PV power system.

The first block represents a set of solar cells (SCs) connected in series / parallel to supply the converter. The solar panel is composed of a certain number of SCs and a string is composed of a series of solar panels. The parallel between strings forms the so-called solar field. The second block is the switch mode DC-DC converter (or DC-AC) which is required to couple the solar cells array with the specific load. Since the output characteristic (current-voltage curve) of an SC is implicit and delivers an unstable Maximum Power Point (MPP) in every given climatic condition, the converter has the role to actively match the output impedance of the SCs array to be very close to the optimum output impedance. The optimum duty cycle is related directly or indirectly to the optimum output impedance, and it is provided to the converter by the Maximum Power Point Tracker (MPPT) algorithm. The load profile depends on the application and can be a combination between ohmic load, batteries, super-capacitor and the grid.

Multi SCs interaction is a fertile topic and is discussed in **Chapter 1**. It can have a significant effect on the solar cell's production, testing process, matched panel, and array design and assembly. The assessment of the parameters of the static SC model was an early investigation; and even nowadays it is still an open research topic, to which this work has contributed through two original methods described in **Chapter 1**. One of the two methods investigated is particularly interesting also for commercial applications such as SCs automatic testing and characterization instruments as described in [1-2].

Since electronic converters apply high frequency solicitations on SCs, the dynamic SC model has been developed and the effect of the parasitic capacitance has been highlighted and justified analytically (**Chapter 1**).

Chapter 2 focuses on MPPT algorithms and topologies. The MPP of the PV power system and the corresponding voltage and current levels keep changing with varying irradiance and solar cells temperature. It, therefore, becomes important to employ MPPT so that the system always operates near MPP. In a typical MPPT system, the PV source is decoupled from the load through a switch mode converter. An algorithm controls the input impedance of the converter to enable tracking of the MPP. This is done directly by controlling the converter's duty cycle, or indirectly by using a voltage / current control loop that continuously sets the converter's reference voltage / current.

In this work, a bridge capacitor interface and its related MPPT algorithm are proposed. The interface has a series of benefits offered by the already being developed MPPT: using a single sensor voltage, presenting a high velocity of convergence, being inductorless, tracking even in high climatic condition variation, and providing the possibility to be integrated.

To overcome the mismatch problems in PV systems, the research trends try to move the MPPT from centralized to a distributed system. Actually, the control of the single panel in a PV system is obtained and commercial examples are shown in [3-4]. The goal is to control the single SC, composing a panel solar individually so it can act as a generator in all conditions.

Chapter 1

SOLAR CELLS MODELS

In this chapter the parameters of the most exploitable static models of solar cells are evaluated using firstly, a sophisticated optimization method in a multi-dimensional variable space which is applied for both single and dual diode models. Secondly, developing a method based on single variable optimization which assesses each parameter from the experimental current-voltage curve with better stability and accuracy. Moreover, the dynamic model is treated to highlight the effect of the capacitance on the output characteristic when it becomes relevant. After that, a motion to create a simple model based on the two environmental parameters (temperature and irradiance) is discussed. Finally, the mismatch effects are revised due to darkening and temperature on a multi-cells model.

1.1 Introduction

Reviews of solar cell (SC) electrical models which differ in complexity are reported in [5]. The single diode model (M-1) of Fig. 1.1 (a), derived from the physics of the p-n junction, is the most used model for SC and is basically adequate to be applied to all silicon SCs.

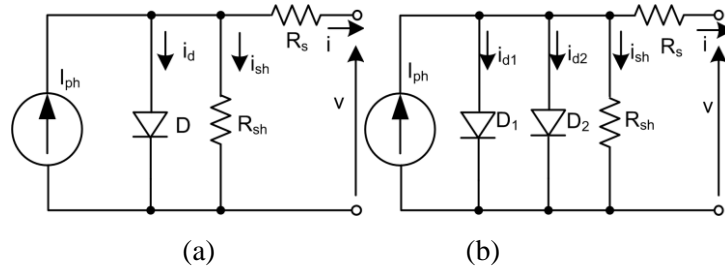


Fig. 1.1 SC static electrical models: (a) with single diode (M-1); (b) with two diodes (M-2).

The characteristic equation for SC (current-voltage relationship) related to M-1 is:

$$i = I_{ph} - i_d - i_{sh} = I_{ph} - I_0 \left(e^{\frac{v + R_s i}{nV_T}} - 1 \right) - \frac{v + R_s i}{R_{sh}} \quad (1.1)$$

where V_T is the thermal voltage, equal to kT/q (k is the Boltzmann constant and equals $1.38066 \cdot 10^{-23}$ J/K, T is temperature of the SC expressed in K and q is the electron charge equals $1.6 \cdot 10^{-19}$ C); I_{ph} is the photocurrent, whose density is

proportional to the number of free electron / hole pairs generated per second; i_d is the diode current and i_{sh} the shunt current; I_0 is the saturation current; n is the ideality factor of the diode; R_s is the series resistance, which represents the resistance of the semiconductor material and of the metal contacts; and R_{sh} is the shunt resistance, which is due to the recombination losses.

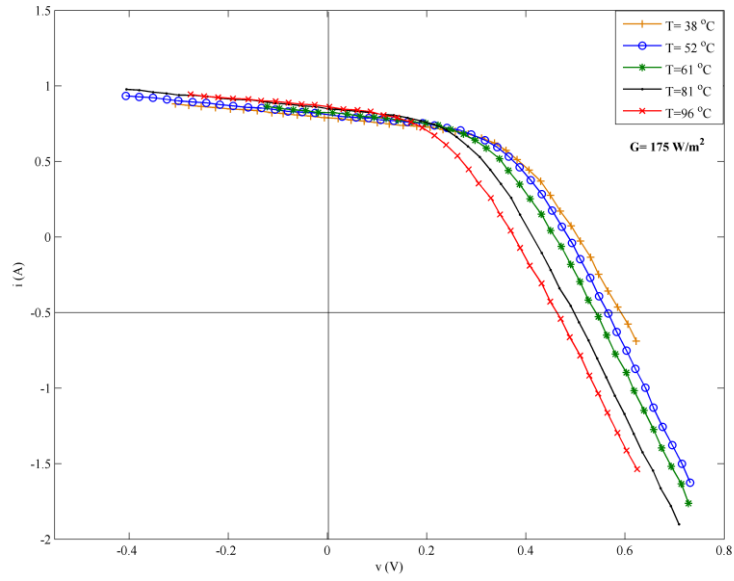
The diode ideality factor has a value between 1 and 2, with n tending to 1 for diodes dominated by recombination in the quasi-neutral regions, and n tending to 2 when recombination in the depletion-region dominates. From here, the dual diode model was developed as shown in Fig. 1.1 (b); where D_1 and D_2 describe the recombination current in the neutral and in the depleted regions respectively. The characteristic equation for this second model is:

$$i = I_{ph} - I_{01} \left(e^{\frac{v+R_s i}{V_T}} - 1 \right) - I_{02} \left(e^{\frac{v+R_s i}{2V_T}} - 1 \right) - \frac{v+R_s i}{R_{sh}} \quad (1.2)$$

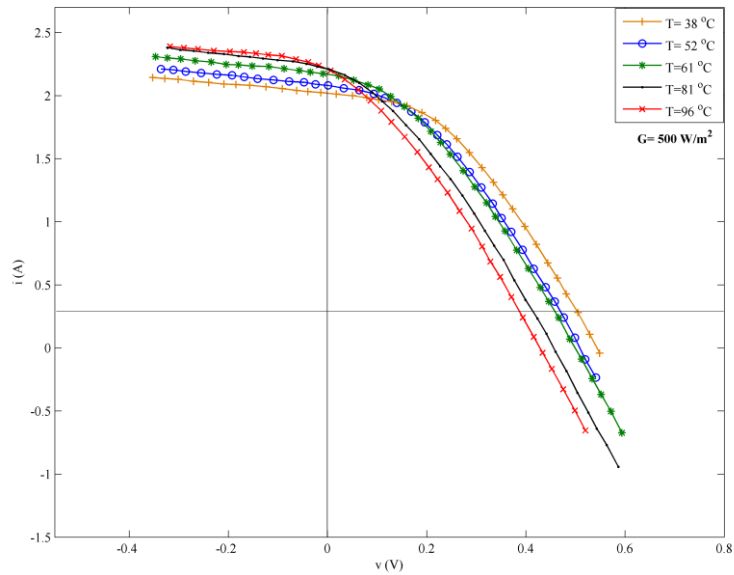
In this way, the two phenomena are directly modeled, rather than being averaged by means of the n parameter. In literature, there is not a study which highlights the difference between the two models. However, the single diode static electrical model is the most exploited and can be applied to most of the actual commercial SC.

To a given irradiance¹ G (W/m^2) and a given temperature T ($^{\circ}C$) of the SC, there corresponds an experimental output characteristic $i-v$ curve. To a given $i-v$ curve, there correspond five parameters for the model in use. Experimental $i-v$ curves for a typical commercial SC are reported in Fig. 1.2 (a) and Fig. 1.2 (b) for five different T at two distinct G . $i-v$ curves are shown in a wide range of operating voltage: the SC acts as a generator in the region between zero voltages up to open circuit voltage. In the other regions, its behavior is as a complex load. From Fig. 1.2, the dependency on G and T of $i-v$ curves is apparent. In particular, the open circuit voltage V_{oc} (at $i=0$) decays with G in a logarithmic manner at fixed T and decays with some $mV/^{\circ}C$ with T at fixed G ; while the short circuit current I_{sc} increases linearly with G at fixed T and

¹ AM1.5 solar irradiation.



(a)



(b)

Fig. 1.2 *i-v* experimental curves at five distinct T equal to 38 °C (‘ ∇ ’ marker), 52 °C (‘ \circ ’ marker), 61 °C (‘*’ marker), 81 °C (‘.’ marker) and 96 °C (‘x’ marker) for two fixed G : (a) G equals to 175 W/m², (b) G equals to 500 W/m². Lines are guide for eye.

increases with T of a few mA at fixed G . In order, increasing T at fixed G the quantities of current gained at the maximum power point MPP (at the knee of the curve) is less than the quantities of the voltage lost at MPP [6]. Taking all effects into account, a decrease of the maximum output power is expected in this condition. Results are shown for V_{oc} , I_{sc} , P_M in Fig.1.3 (a), Fig.1.3 (b) and Fig.1.3 (c), respectively.

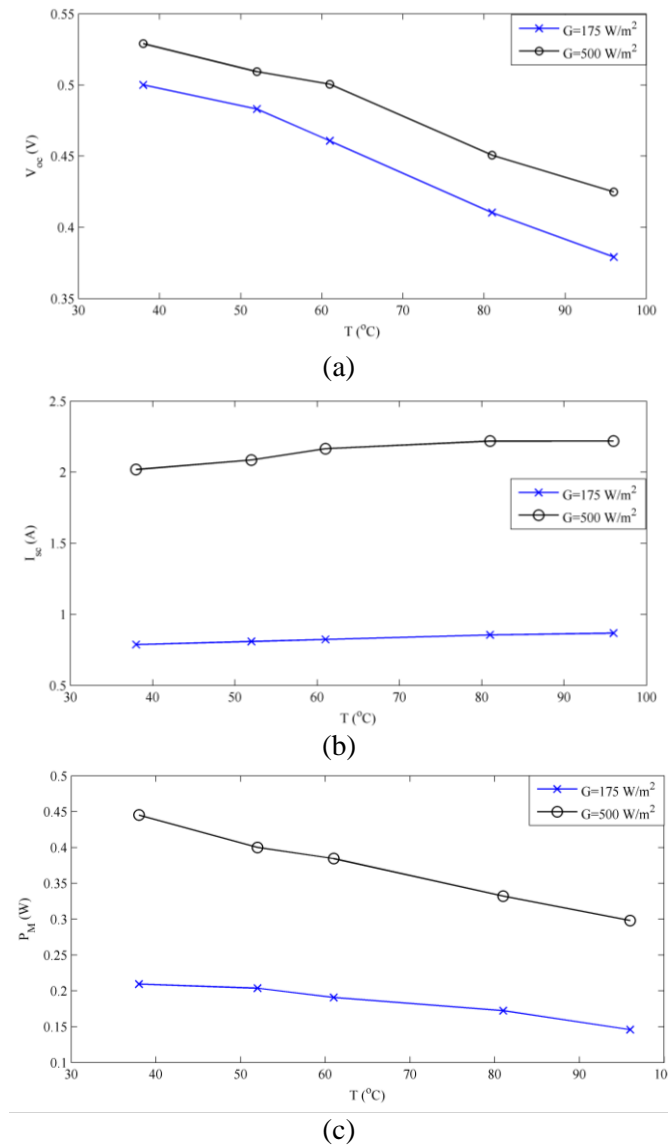


Fig. 1.3 Variation of the open circuit voltage, short circuit voltage and the maximum power with the climatic parameters (G and T). (a) V_{oc} (b) I_{sc} (c) P_M .

As Silicon SCs capacitance is in the range 40 nF/cm^2 per cell, an analysis of the dynamic model, shown in Fig. 1.4, is performed. In addition with respect to the static model, it includes the parasitic capacitance c_p which embeds the transition and diffusion capacitance.

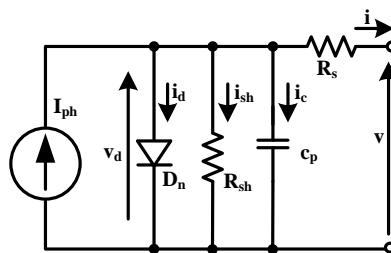


Fig. 1.4 Single diode dynamic electrical model of SC

The characteristic equation for the dynamic model is defined as follows:

$$\begin{aligned}
 i &= I_{ph} - i_d - i_{sh} - i_{c_p} \\
 &= I_{ph} - I_0 \left(e^{\frac{v + R_s i}{n V_T}} - 1 \right) - \frac{v + R_s i}{R_{sh}} - c_p \frac{\partial(v + R_s i)}{\partial t} - (v + R_s i) \frac{\partial c_p}{\partial t}
 \end{aligned} \tag{1.3}$$

Even if c_p presents a small value; its effects should be taken into account when transients are sufficiently fast. For silicon SC, the capacitive effect can be relevant on the output characteristic, as can be seen in Fig 1.5, when it is characterized or electronically biased at high frequency:

- to qualify SCs, flash testing techniques (20ms) are widespread since quasi-static temperature testing can be performed [7];
- to maintain the SC to the optimum operating voltage where maximum output power is obtained, independently of external conditions: efficient SC output decoupling from actual load is performed with high frequency switching (several kHz) converters equipped with fast load matching maximum power point tracker systems [8].

For dye-sensitized SCs, the capacitance effects are relevant at low bias frequency and have a high value of c_p [9].

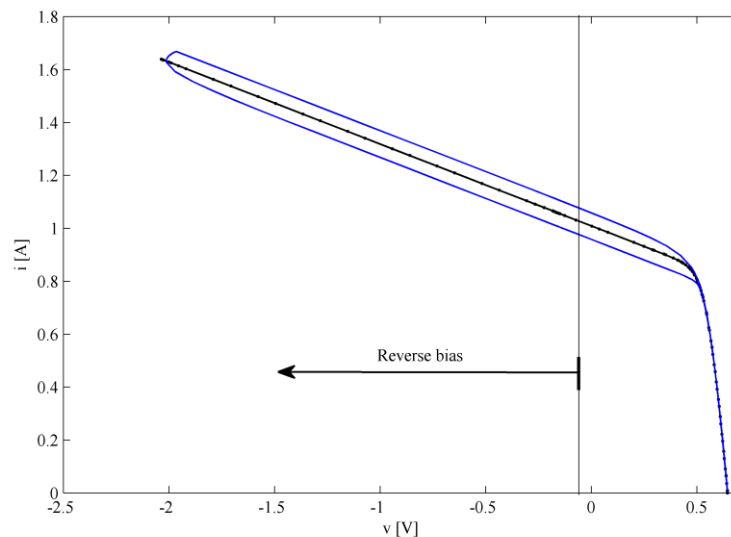


Fig 1.5 i - v curve for the static (‘.’ marker) and dynamic model (solid line with no marker)

1.2 Methods of description for parameters evaluation.

Accurate SC simulation [6, 10], SC testing and characterizing [1, 2], SC study and analyzing of performance [11] and model-based maximum power point trackers (MPPT) technique [12, 13] require knowledge of the model parameters employed. The unknown electrical parameters for M-1 and for M-2 are I_{ph} , I_0 , n , R_s , R_{sh} and I_{ph} , I_{01} , I_{02} , R_s , R_{sh} , respectively. The characteristic equation is implicit and non linear. Therefore, a determination of an analytical solution of the parameters evaluation is a complex problem and a summary from the literature is given as follows:

Some methods use measurements of the illuminated $i-v$ characteristics at a single, or at different levels of lighting [14-17], some use only dark conditions [18-19], while others utilize dark and lighted measurements [20-21]. The methods in [14-21] are developed under the assumption that SC parameters do not depend on the environmental parameters G and T . Moreover, they consider only I_0 or R_s as parameters, assuming R_{sh} is infinite, idealizing n and approximating I_{ph} to the short current. This simplification and approximation leads to models which are not representative of actual SC behavior. To overcome that, sophisticated methods have been developed and they are based on the optimization of the five parameters, and they often present convergence and stability problems and can present non physical values of the parameters. Vertical Optimization Method (VOM) based on an approach that minimizes error on the vertical axis (i.e, the current) and Lateral Optimization Method (LOM) based on the approach of minimizing error on the lateral axis (i.e, the voltage) are presented in [22] and [23] respectively.

To take account of both, the current and voltage error measurements, a procedure called APTIV is presented in [24]. It is based on separate least-squares fitting in two different regions (current fitting near the short circuit and voltage fitting near the open-circuit). However, the accuracy of the APTIV method depends on the soundness of the fitting used (i.e. how the equation adopted in both regions represents the real output curve of the SC).

A genetic algorithms and particle swarm optimization has been proposed, also, as can be seen in [25-26].

In this thesis, we propose two methods to assess the parameters of the single / dual diode electrical model of SC. The first one [27] is an iterative method, using Newton-Raphson, which permits to evaluate simultaneously all the parameters without any approximation. The second one [28] is a method which reduces the optimization to a mono-dimensional variable space and evaluates singularly the parameters, where their own effect dominates by a simple fitting corresponding to their physical effect (i.e. linear for resistances and exponential for diode parameters). After that, an analysis to estimate the capacitance [29] for the dynamic model is provided.

1.2.1 Newton-Raphson method (N-R)

To find these five unknown parameters, a system of five independent equations has to be written. This system is obtained considering the characteristic equation in five distinct working points on an experimental $i-v$ curve. For example, an extracted $i-v$ curve in given fixed illumination ($G=105 \text{ W/m}^2$) and fixed temperature conditions ($T=22 \text{ }^\circ\text{C}$) is shown in Fig. 1.6.

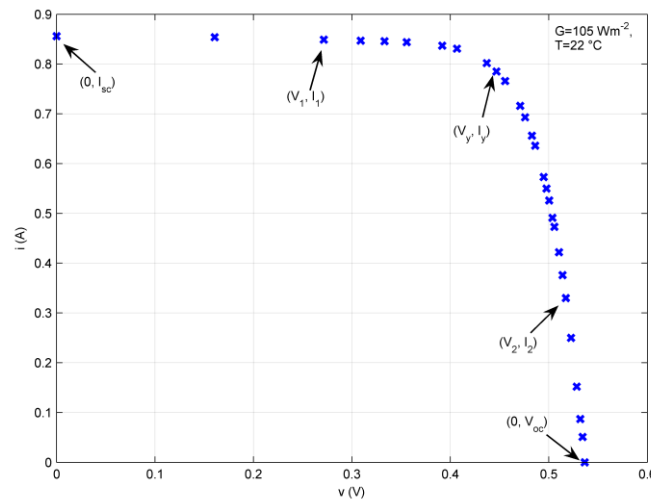


Fig. 1.6 Experimental SC $i-v$ curve shown at fixed climatic conditions.

The five distinct working points are taken in a distributed manner from $i-v$ curve of Fig. 1.6:

- $(0, I_{sc})$ is the short circuit point;
- (V_1, I_1) belongs to the quasi-flat region where the SC operates like a current generator;
- (V_y, I_y) belongs to the knee zone which separates the quasi-flat and the descendant zone;

- (V_2, I_2) belongs to the descendent branch where the SC operates like a voltage generator;
- $(V_{oc}, 0)$ is the open circuit voltage.

Replacing the five operating points in equation (1.1) leads to system (I) composed by equations (1.4) to (1.8) and shown in the following:

$$f_1(\bar{x}) = I_{ph} - I_{sc} \left(1 + \frac{R_s}{R_{sh}}\right) + I_0 - I_0 e^{\left(\frac{R_s I_{sc}}{n V_T}\right)} = 0 \quad (1.4)$$

$$f_2(\bar{x}) = I_{ph} - I_1 \left(1 + \frac{R_s}{R_{sh}}\right) + I_0 - I_0 e^{\left(\frac{R_s I_1 + V_1}{n V_T}\right)} - \frac{V_1}{R_{sh}} = 0 \quad (1.5)$$

$$f_3(\bar{x}) = I_{ph} - I_M \left(1 + \frac{R_s}{R_{sh}}\right) + I_0 - I_0 e^{\left(\frac{R_s I_M + V_M}{n V_T}\right)} - \frac{V_M}{R_{sh}} = 0 \quad (1.6)$$

$$f_4(\bar{x}) = I_{ph} - I_2 \left(1 + \frac{R_s}{R_{sh}}\right) + I_0 - I_0 e^{\left(\frac{R_s I_2 + V_2}{n V_T}\right)} - \frac{V_2}{R_{sh}} = 0 \quad (1.7)$$

$$f_5(\bar{x}) = I_{ph} + I_0 - I_0 e^{\left(\frac{V_{oc}}{n V_T}\right)} - \frac{V_{oc}}{R_{sh}} = 0 \quad (1.8)$$

The characteristic equation is implicit and cannot be solved by simple substitution. An iterative method can be used to extract the real values of the unknown parameters with a good approximation. Newton-Raphson (N-R) method is characterized by a fast convergence, which consists of finding a solution to \bar{x}_{k+1} from \bar{x}_k using the following formula:

$$\bar{x}_{k+1} = \bar{x}_k - \frac{F(\bar{x}_k)}{J_F(\bar{x}_k)} \quad (1.9)$$

where \bar{x}_k and \bar{x}_{k+1} are the vectors containing the parameters calculated at the k , $k+1$ iterations, respectively; $F(\bar{x}_k)$ is the functional of the system (I) shown above, i.e:

$$F(\bar{x}_k) = (f_1(\bar{x}_k) f_2(\bar{x}_k) f_3(\bar{x}_k) f_4(\bar{x}_k) f_5(\bar{x}_k))^T \quad (1.10)$$

and $J_F(\bar{x}_k)$ is the corresponding Jacobian matrix of $F(\bar{x}_k)$.

If condition 1 (C_1) and condition 2 (C_2) are both satisfied:

$$\left\| \frac{\bar{x}_{k+1} - \bar{x}_k}{x_1} \right\| < \varepsilon \quad (C_1)$$

$$\left\| \frac{F(\bar{x}_k)}{F(\bar{x}_1)} \right\| < \varepsilon \quad (C_2)$$

then, the iterative method ends and gives the value of the parameters. C_1 is the module of the difference between the values of the parameters at 'k+1' and 'k' iterations, normalized to the starting point. It indicates the convergence of the problem. Indeed, to assure that the solution converges to a real value, C_2 must also be verified. This condition reflects the fact that the value of the functional tends to zero. We should note that the smaller ε is, the more accurate the value of the parameters at the expense of convergence.

Before the application of the method, some simplifications should be made. Observing system (I), it is possible to eliminate the I_{ph} parameter by subtracting equation (1.4) from (1.5), (1.6), (1.7) and (1.8). After this operation, the system is reduced to four-by-four. In this way, I_0 , R_s , R_{sh} and n can be determined. I_{ph} is then deduced by solving (1.4). The starting points must have a physical meaning: R_s , R_{sh} , I_0 , I_{01} and I_{02} should have positive values, and n between 1 and 2. For the present work, R_{sh} is derived from the linear approximation between $(0, I_{sc})$ and (V_1, I_1) ; R_s via the linear approximation between (V_2, I_2) and $(V_{oc}, 0)$; n equals to 1; I_0 and I_{01} (for M-2) equal to 10^{-9} and I_{02} (for M-2) equals to 10^{-7} .

The system presents a convergence problem related to the Jacobean matrix adopted by applying the N-R method. This problem is due to the large arguments of the exponential present in equation 1. To overcome this problem, the equations of the reduced system were multiplied by $\exp(-(v_x + R_s i_x)/(2nV_T))$, where (v_x, i_x) represents the considered working point. This operation allows the exponential terms to be bounded, thus producing convergence. The same procedure was applied to M-2 by reducing the system to four-by-four, by arranging the equation, and by multiplying it by $\exp(-(v_x + R_s i_x)/(2V_T))$.

1.2.2 Single variable optimization method (SVO)

The key idea is to reduce the optimization process to a single variable R_s , which has upper bound constrained due to SC impedance behavior, thus greatly reducing optimization difficulties. R_s is extracted from the $i-v$ curve for voltage higher than diode threshold voltage; R_{sh} and I_{ph} are calculated from the reverse zone. I_0 and n are deduced by an exponential fitting using the direct diode zone. Owing to cell impedance curve monotonic behavior, optimization of the model's parameters is straightforward as R^2 (coefficient of determination which is defined in **section 1.4**) presents a single maximum depending on R_s . The incremental conductance g is defined in equation 1.11 and an example is plotted in Fig. 1.7.

$$g = \frac{\partial i}{\partial v} = \frac{\frac{1}{R_{sh}} + \frac{I_0}{nV_T} \left(e^{\frac{v+R_s i}{nV_T}} \right)}{1 + R_s \frac{I_0}{nV_T} \left(e^{\frac{v+R_s i}{nV_T}} \right) + \frac{R_s}{R_{sh}}} \quad (1.11)$$

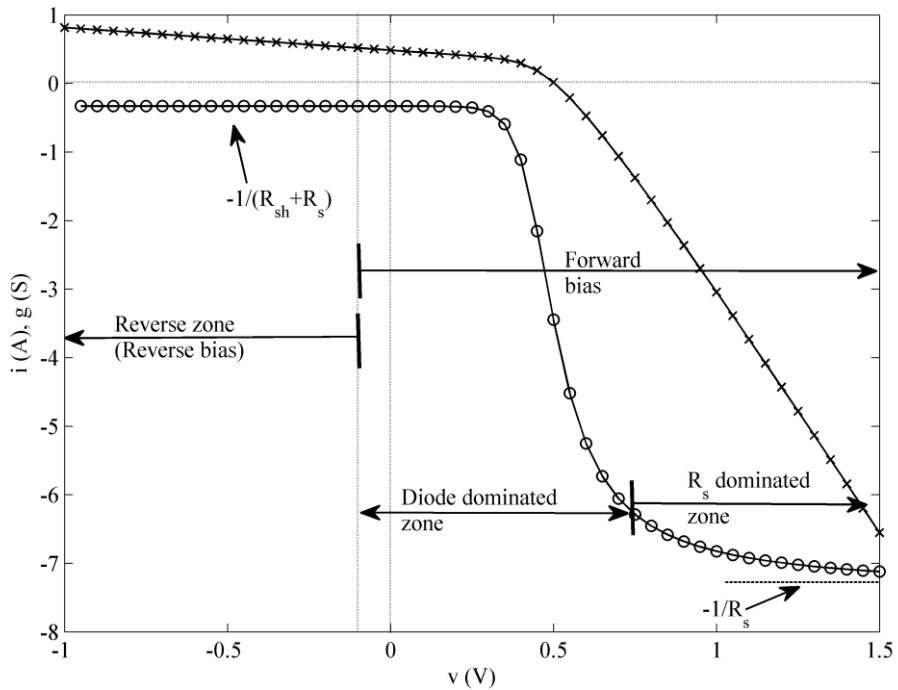


Fig. 1.7 $i-v$ curve ('x' marker) with the respective incremental conductance ('o' marker)

Depending on the output voltage v , three cases corresponding to the three zones shown in Fig.1.6 can be distinguished:

- a) reverse zone case where the function g is equal to $(-1/(R_s+R_{sh}))$;
- b) diode dominated zone where diode forward bias produces a fast change of g ;
- c) R_s dominated zone where function g tends asymptotically to $(-1/R_s)$ value.

The R_s influence in reverse zone and R_s dominated zone is straightforward. The diode i_d-v_d curve can be extracted and exponential-like behavior appears when the proper R_s is chosen, greatly effecting I_0 and n evaluation. Parameters R_{sh} and I_{ph} immediately follow with a linear fitting of the reverse zone available $i-v$ curve. After this operation, the diode i_d-v_d curve is calculated and diode parameters are extracted with an exponential fitting from forward bias available data. Model fit is evaluated with R^2 and a new candidate for R_s is chosen using an optimization method. The procedure is repeated until the maximum of R^2 is found. The flow-chart algorithm related to single variable optimization (SVO) method is shown in Fig. 1.8 and the extension to the double diode model is straightforward.

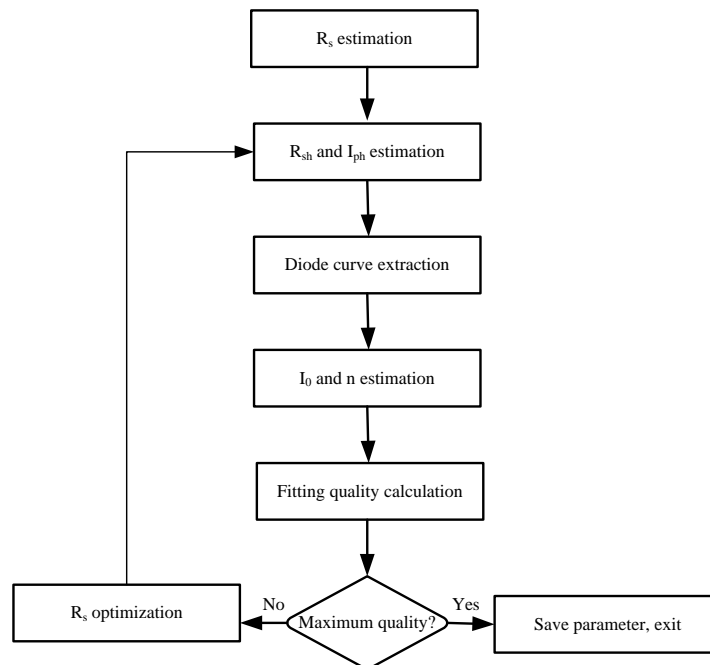


Fig. 1.8 Flow-chart algorithm related to SVO method

1.2.3 Capacitance estimation

The incremental conductance of the SC explains the different behavior of the output characteristic during rising and falling current sweep. For the dynamic model, it is defined as follows:

$$\begin{aligned}
 g &= \frac{\partial i}{\partial v} \\
 &= - \frac{\frac{1}{R_{sh}} + \frac{I_0}{nV_T} \left(e^{\frac{v+R_s i}{nV_T}} \right)}{1 + R_s \frac{I_0}{nV_T} \left(e^{\frac{v+R_s i}{nV_T}} \right) + \frac{R_s}{R_{sh}} + R_s \frac{\partial c_p}{\partial t}} \quad (1.12) \\
 &\quad \frac{\frac{\partial c_p}{\partial v} \frac{\partial (v+R_s i)}{\partial t} + c_p \frac{\partial^2 (v+R_s i)}{\partial v \partial t} + (v+R_s i) \frac{\partial^2 c_p}{\partial v \partial t} + \frac{\partial c_p}{\partial t}}{1 + R_s \frac{I_0}{nV_T} \left(e^{\frac{v+R_s i}{nV_T}} \right) + \frac{R_s}{R_{sh}} + R_s \frac{\partial c_p}{\partial t}}
 \end{aligned}$$

The effect of the capacitance is relevant for high $\partial v/\partial t$ and the diode effect tends to cancel all terms but $1/R_s$. For this reason, the effect is investigated in reverse zone referring to the model shown in Fig. 1.9.

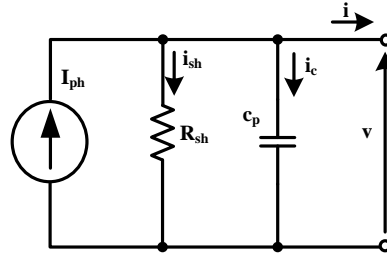


Fig. 1.9 SC dynamic electrical model in reverse zone.

In this case, the incremental conductance becomes:

$$g = \frac{\partial i}{\partial v} = - \left(\frac{1}{R_{sh}} + \frac{\partial c_p}{\partial v} \frac{\partial v}{\partial t} + c_p \frac{\partial^2 v}{\partial v \partial t} + v \frac{\partial^2 c_p}{\partial v \partial t} + \frac{\partial c_p}{\partial t} \right) \quad (1.13)$$

As shown in equation 1.13, the incremental conductance accounts for the static term $1/R_{sh}$ and dynamic terms, which feature opposite sign for the rising and the falling edge of the current sweep. An adequate choice of the forcing function can help recognizing the various terms involved in the dynamic component of the incremental conductance.

Capacitance is estimated exploiting the splitting of the output characteristic due to the charge and discharge effect. In the reverse zone, the static parameters are given by

the sum between the series and shunt resistance. Generally, the series resistance R_s is orders of magnitude smaller than the shunt resistance; therefore, for this analysis it is neglected. For a given climatic condition, the output characteristic can be expressed as:

$$i_1 = I_{ph} - \frac{v}{R_{sh}} - c_p \left(\frac{\partial v}{\partial t} \right)_1 - v \frac{\partial c_p}{\partial t}; \text{ for } \frac{\partial v}{\partial t} < 0 \quad (1.14)$$

$$i_2 = I_{ph} - \frac{v}{R_{sh}} - c_p \left(\frac{\partial v}{\partial t} \right)_2 - v \frac{\partial c_p}{\partial t}; \text{ for } \frac{\partial v}{\partial t} > 0 \quad (1.15)$$

where i_1 refers to the output characteristic curve during the rising edge of the current sweep while i_2 refers to the falling edge.

From (1.14) and (1.15), the capacitance can be obtained as:

$$c_p = \frac{i_1 - i_2}{\left(\frac{\partial v}{\partial t} \right)_2 - \left(\frac{\partial v}{\partial t} \right)_1} \quad (1.16)$$

As it can be seen from (1.16), the separation between rising and falling current sweep output characteristic is justified by the presence of the parasitic capacitance c_p .

1.3 Experimental setup

Distinct methods to characterize the SC have been used when different experimental setups were developed. The N-R method was investigated using a standard variable resistance load. When the SVO method was developed, the need for a flexible and automatic loading system aroused and the same system was applied for the dynamic model test.

1.3.1 Newton-Raphson

The measurements were performed in the field and a polycrystalline SC (156 mm × 156 mm) was employed. Under standard test condition, this SC presents the following electrical data: V_{oc} , 0.61 V; I_{sc} , 8.3 A; V_M , 0.5 V; I_M , 7.5 A where V_M and I_M are the voltage and current at maximum output power respectively. A load rheostat to vary the output voltage and consequently statically characterize the SC is used. The acquisition is performed using a digital voltmeter (accuracy $\pm 0.5\%$) and a digital ammeter ($\pm 0.4\%$). It was equipped with a GPIB card for direct interface with a personal computer to save the output voltage and output current of the SC respectively. Finally, a thermocouple ($\pm 2\text{ }^\circ\text{C}$) and a commercial radiation meter ($\pm 3\%$) are used to record the temperature of the SC and to detect the irradiance at the surface of the SC respectively.

1.3.2 Single variable optimization

A commercial monocrystalline solar cell (125×125 mm) is used. The electrical data, under standard test conditions, are: P_M , 2.06 W; I_M , 4.33 A; V_M , 0.475 V. A current sweep circuit was employed to bias it as shown in Fig. 1.10: a function generator is used as reference for the power amplifier (v_{ref}), which drives the SC; the output current (i) is imposed through feedback of R_{sense} ($1.62\ \Omega \pm 0.01$).

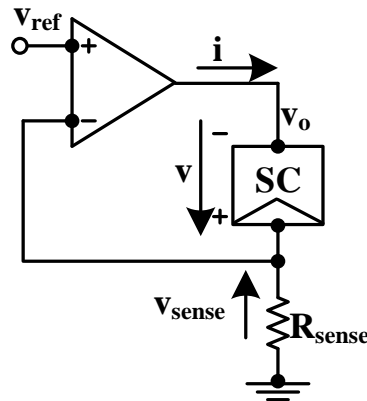


Fig. 1.10 Current sweep circuit.

The input signal (v_{ref}), the sensing voltage (v_{sense}) and the amplifier output voltage (v_o) are acquired with a digital oscilloscope (100 MHz bandwidth limited for noise rejection). The output voltage of SC can be deduced by the difference between v_{sense} and v_o . This topology allows for:

- four quadrant operation using an arbitrary reference
- fast measurement for quasi-static temperature condition on SC
- low and high frequency to characterize the SC with an electronic load statically and dynamically respectively.

The same measurement setup is employed to bias the SC at high frequency when the effect of the parasitic capacitance becomes relevant. In this case, measurements were done inside laboratory using a 500 W halogen lamp which has a spectrum closes to the solar one.

1.4 Methods validation.

The N-R method is applied to identify the parameters for both static model M-1 and M-2. Ten different measurements were examined in a wide range of climatic conditions. The method's resistance to measurement noise is tested.

The SVO method is applied to identify the M-1 parameters in both dark and illuminated conditions. Dynamic model is used to estimate capacitance for three distinct measurements at the same climatic condition which differs from the frequency of the bias voltage.

1.4.1 Newton-Raphson

At a given irradiance (G) and a given temperature (T), the SC presents a unique output characteristic and consequently a set of associated parameters. Ten different cases were examined where measurements of environment conditions are shown in [Fig. 1.11](#) through the map (G, T). Three of the ten measurements are considered at the same temperature, two at the same irradiance and five are distributed along a typical operation condition of an SC; G ($45 \div 1000$) Wm^{-2} and T ($14 \div 46$) $^{\circ}\text{C}$.

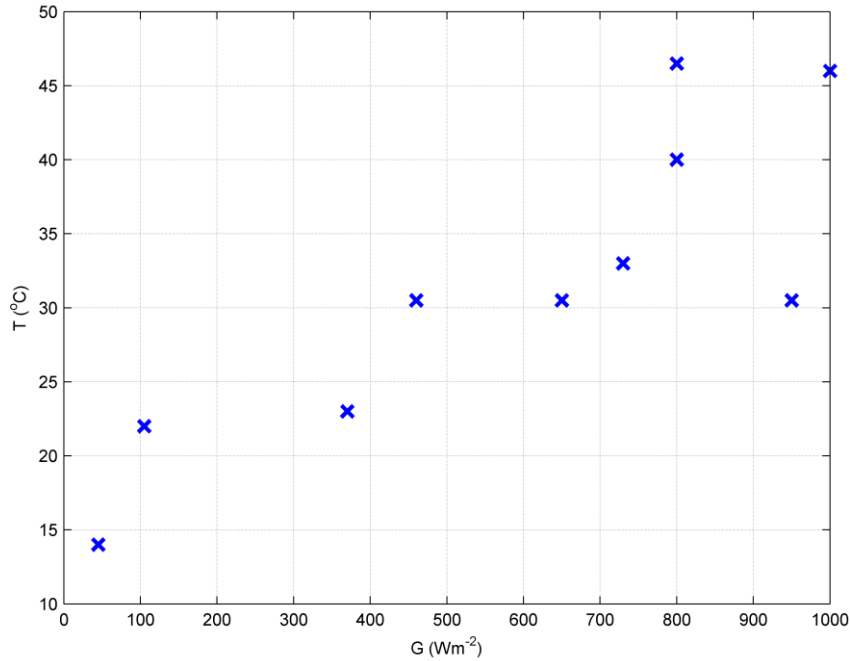


Fig. 1.11 Climatic condition measurements map; x indicates the climatic conditions in which the measurements have been performed.

In Table 1 and Table 2, the value of the parameters obtained for the ten measurements is reported for M-1 and M-2 respectively. The first line and the first column of each table report the value of the climatic condition and the corresponding parameters respectively. The two models considered differ in the model of the diode adopted. As can be seen from Table 1.1 and 1.2, both models present almost the same I_{ph} , R_s and R_{sh} in a given condition.

Table 1.1: M-1 SC parameters found for ten distinct measurements.

G (Wm ⁻²), T (°C)	G ₁ =450 T ₁ =30.5	G ₂ =650, T ₂ =30.5	G ₃ =950 T ₃ =30.5	G ₄ =800 T ₄ =40	G ₅ =800 T ₅ =46.5	G ₆ =45, T ₆ =14	G ₇ =105, T ₇ =22	G ₈ =370 T ₈ =23	G ₉ =730 T ₉ =33	G ₁₀ =1000 T ₁₀ =46
I_{ph} (A)	3.771	5.395	7.69	6.665	6.648	0.333	0.856	2.907	6.076	8.364
I_0 (A)	4.48e-9	1.08e-8	1.12e-7	1.38e-7	1.95e-7	1.48e-8	8.86e-9	2.72e-8	1.56e-8	6.02e-7
R_s (Ω)	0.0155	0.0164	0.0155	0.0144	0.0177	0.0087	0.0146	0.0174	0.0167	0.0156
R_{sh} (Ω)	5.27	2.51	3.2	3.93	8.24	34.07	36.91	10.43	2.23	3.38
n	1.03	1.08	1.2	1.15	1.11	1.24	1.15	1.17	1.07	1.19

Table 1.2: M-2 parameters found for ten distinct measurements.

G (Wm ⁻²), T (°C)	G ₁ =450 T ₁ =30.5	G ₂ =650, T ₂ =30.5	G ₃ =950 T ₃ =30.5	G ₄ =800 T ₄ =40	G ₅ =800 T ₅ =46.5	G ₆ =45, T ₆ =14	G ₇ =105, T ₇ =22	G ₈ =370 T ₈ =23	G ₉ =730 T ₉ =33	G ₁₀ =1000 T ₁₀ =46
I_{ph} (A)	3.776	5.403	7.702	6.669	6.651	0.334	0.857	2.911	6.087	8.381
I_{01} (A)	2.21e-9	2.15e-9	2.73e-9	7.64e-9	2.39e-8	1.9e-10	5.3e-10	7.1e-10	3e-9	1.82e-8
I_{02} (A)	1.53e-6	4.19e-6	2e-6	3.33e-5	4.93e-5	1.7e-6	2.3e-6	7.6e-6	8.25e-6	6.9e-5
R_s (Ω)	0.0157	0.0167	0.0167	0.0148	0.018	0.0198	0.0176	0.0183	0.0169	0.016
R_{sh} (Ω)	5.28	2.53	3.42	4.9	8.16	33.94	46.4	8.91	2.2	3.26

A further analysis was performed to verify how the method is affected by noise. For this purpose, noise was introduced on the values of the operating voltage / current in the following manner:

$$z_{\text{noise}} = z_{\text{no_noise}}(1 + \lambda \cdot \xi) \quad (1.17)$$

where $z_{\text{no_noise}}$ is the reference voltage or current and z_{noise} is the voltage or current including noise used in the procedure of determination of the parameters. ξ is a randomly generated number between -1 and +1. λ is the relative percentage of error to be added. The λ considered was 0.1 %, 0.5 %, 1 %, 5 % and 10 %. The reference curve is extracted from the parameters related to ($G_1=450 \text{ Wm}^{-2}$, $T_1=30.5 \text{ }^\circ\text{C}$) conditions.

For all λ considered, 200 sets of working points have been generated, each with independent random voltage and current. A statistical analysis of the 200 sets of parameters connected to a given noise is performed. In Fig 1.12, a histogram is reported for the 0.1 % case, and in Table 1.3, the mean value (\bar{p}) and the standard deviation (σ) are reported for all percent considered.

Table 1.3: parameters evaluated with noise.

No noise	Noise=0.1%		Noise=0.5%		Noise=1%		Noise=5%		Noise=10%	
Parameters	\bar{p}	σ	\bar{p}	σ	\bar{p}	σ	\bar{p}	σ	\bar{p}	σ
I_{ph} (A)	3.77	3.46e-3	3.77	5e-3	3.77	8e-3	3.81	0.1	3.93	1.85e-1
I_0 (A)	4.21e-9	1.90e-9	5.2e-9	2.46e-9	1.12e-7	1.99e-7	3.53e-6	9.33e-6	1.32e-6	3.46e-6
R_s (Ω)	0.0155	3.74e-4	0.015	2.33e-3	0.0132	2.36e-3	0.0102	6.31e-3	0.0148	8.6e-3
R_{sh} (Ω)	5.224	3.32e-1	5.668	1.38e-1	6.971	3.97e-1	3.563	2.76e-1	2.408	4.38e-1
n	1.03	1.87e-2	1.08	2.73e-2	1.15	0.1	1.3	0.22	1.17	1.73e-1

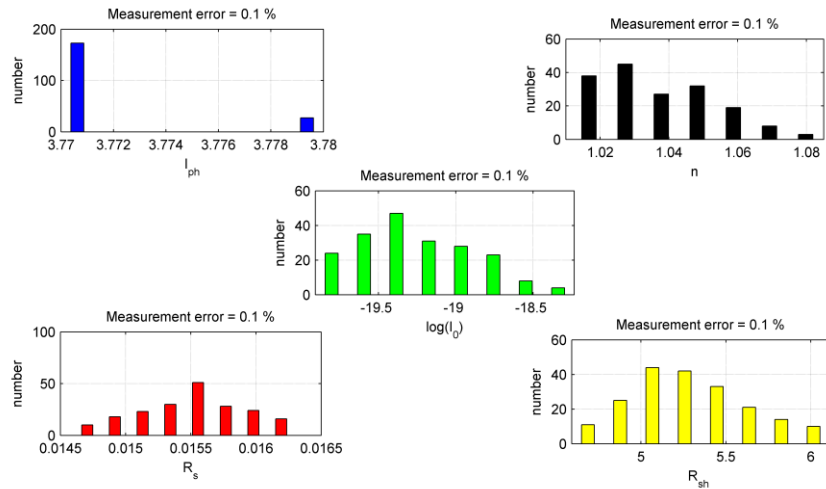


Fig. 1.12 Histogram of the parameters statistical distribution with percent equals to 0.001 (0.1 % of noise).

1.4.2 Single variable optimization

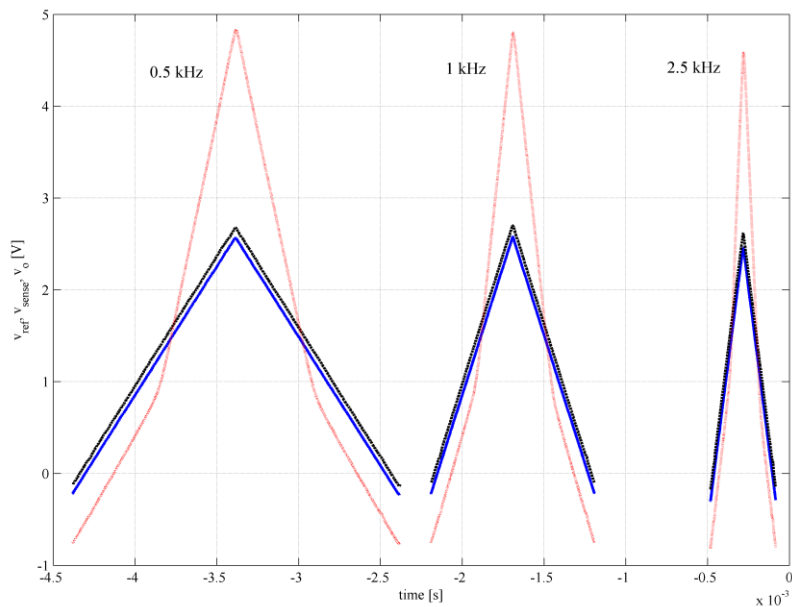
The parameters evaluation of M-1 from experimental $i-v$ curves are applied for two different measurements: the first was done on dark condition at a T equal to 27 °C and the second was done in the field at irradiance G equal to 345 Wm⁻² and T equal to 36 °C. The obtained results are shown in Table 1.4. This method is efficient in both dark and illuminated conditions and a coefficient of determination obtained is higher then 0.9999 as we will see in the next section.

Table 1.4: *parameters found for the two distinct measurements.*

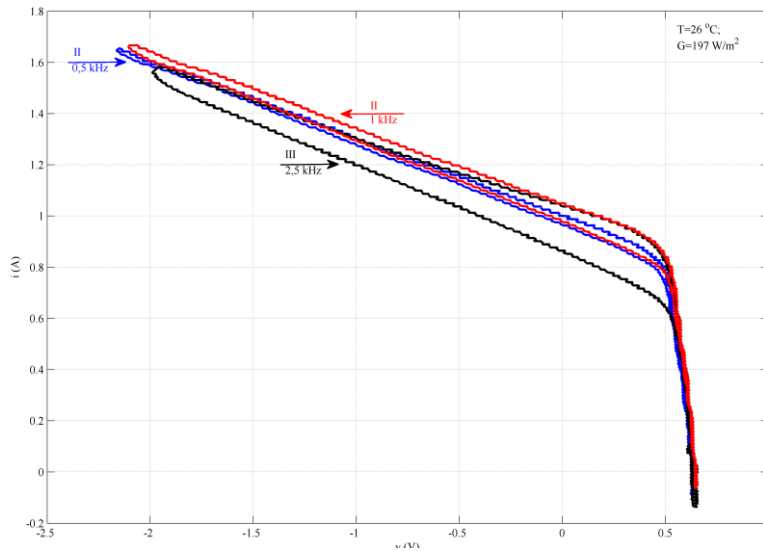
	G=0 Wm ⁻² , T=27 °C	G=345 Wm ⁻² , T=36 °C 36°C
R _s (Ω)	0.173	0.124
R _{sh} (Ω)	2.849	2.783
I _{ph} (A)	0.01	1.447
I ₀ (A)	2.13e ⁻⁷	3.34e ⁻⁷
n	1.438	1.308

1.4.3 Capacitance estimation

At a fixed climatic condition (T=26 °C, G=197 W/m²), three distinct measurements were performed which differ in the frequency of the bias signal. The input signal V_{ref} was an ascendant/descendant ramp with a frequency equal to 0.5 kHz, 1 kHz and 2.5 kHz. From time data shown in Fig. 1.13 (a), the output characteristic $i-v$ is extracted as shown in Fig. 1.13 (b). At low frequency, the phenomenon is not relevant and the output characteristic is quasi unique (curve I). As the frequency increases, the charge



(a)



(b)

Fig. 1.13 (a) The experimental acquired signal v_{ref} (solid line), v_{sense} (dashed line), and v_o (dotted line) in time domain; (b) $i-v$ curve at three different frequency of bias (curve I at 0.5kHz, curve II at 1 kHz and curve III at 2.5 kHz).

and discharge effect of the capacitor becomes visible, splitting the output characteristic (curves II and III). Using the analysis developed in **Section 1.2**, an estimation of the capacitance was done in reverse zone. A linear dependency with the output voltage was found.

The results are reported in **Table 1.5** for the three different cases. In order to complete the analysis the evaluation of the five static parameters were done using the method developed in [30] and results are reported in **Table 1.6**.

Table 1.5: capacitance estimation

Frequency [kHz]	c_p [μ F]
0,5	$0,687 \cdot v + 2,951$
1	$0,779 \cdot v + 2,891$
2,5	$0,882 \cdot v + 2,877$

Table 1.6: static parameters determination at 26 °C and 197 W/m²

Parameters	values
I_{ph} (A)	1.035
I_0 (A)	$1.05e^{-10}$
n	1.12
R_s (Ω)	0.08
R_{sh} (Ω)	3.15

1.5 Methods application

Methods qualities are verified by comparing the calculated i - v curves obtained from the evaluated parameters and their related experimental one. For this purpose the SC mathematical models have been reproduced using Matlab / Simulink, Matlab / M-file and Matlab / Simscape to validate N-R method, SVO method and the capacitance estimation, respectively. The choice of the type of implementation is irrelevant; it permits to see some possible ways to implement the implicit characteristic equation of the SC.

The models quality is evaluated through the coefficient of determination R^2 . It is defined as follows:

$$R^2 = 1 - \frac{RSS}{TSS} \quad (1.18)$$

where RSS and TSS are the residual sum of squares and the total sum of squares, respectively:

$$RSS = \sum_{i=1}^N (i_i - i_{sim-i})^2 \quad (1.19)$$

$$TSS = \sum_{i=1}^N (i_i - i_m)^2 \quad (1.20)$$

where i_i is the measured current at the i -th point among N measurements considered; i_{sim-i} is the simulated current at the same i -th point and i_m is the mean of the measured current.

1.5.1 Newton-Raphson

A mathematical model has been developed in Simulink. It is based on equation (1.1) and equation (1.2) for M-1 and M-2, respectively. The system implementation for M-1 is shown in Fig. 1.14. The proposed model takes the calculated parameters (I_{ph} , I_0 , n , R_s and R_{sh}) and the temperature of the SC as input and i - v characteristic is delivered as output. Simulations were done for the same values of load used in the experiments test. Results for the ten measurements (Section 1.4) are shown in Fig. 1.15 (a) for M-1 and in Fig. 1.15 (b) for M-2. R^2 obtained is reported in Table 1.7.

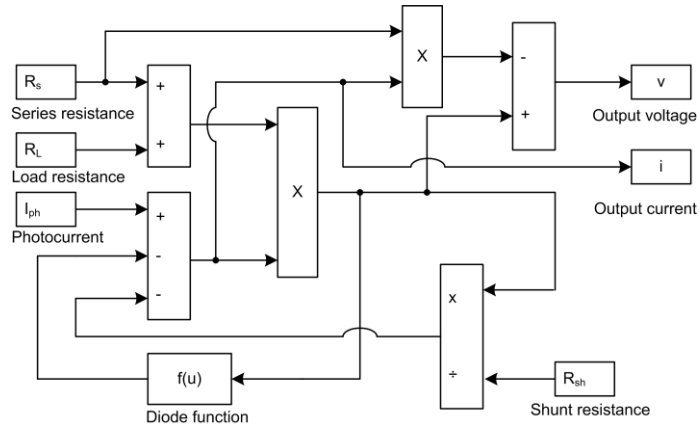


Fig. 1.14 Simulink implementation of SC for M-1.

Table 7: R^2 values calculated for M-1 and M-2.

Condition : G (Wm^{-2}), T ($^{\circ}\text{C}$)	$G_1=450$ $T_1=30.5$	$G_2=650$, $T_2=30.5$	$G_3=950$, $T_3=30.5$	$G_4=800$, $T_4=40$	$G_5=800$, $T_5=46.5$	$G_6=45$, $T_6=14$	$G_7=105$, $T_7=22$	$G_8=370$, $T_8=23$	$G_9=730$, $T_9=33$	$G_{10}=1000$, $T_{10}=46$
$R^2(\text{Experimental}/$ $M-1)$	0.9995	0.9993	0.9994	0.9992	0.9993	0.9993	0.9994	0.9993	0.9992	0.9991
$R^2(\text{Experimental}/$ $M-2)$	0.9994	0.9993	0.9994	0.9992	0.9993	0.9992	0.9994	0.9993	0.9992	0.999

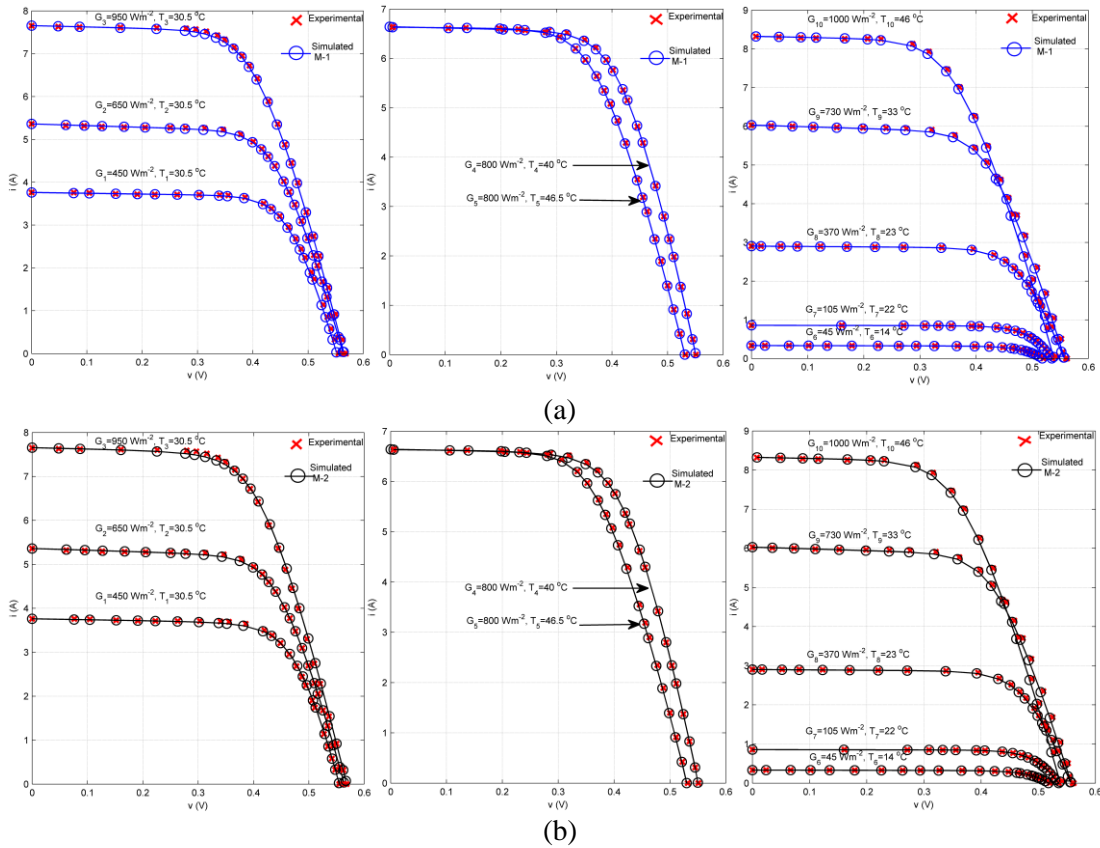


Fig. 1.15 Experimental ('x' marker) and simulated curve (solid line with 'o' marker); (a) M-1; (b) M-2

1.5.2 Single variable optimization

SVO method is applied using an M-file. The problem's description is reported in the following equations (1.21-1.24).

For a giving wide range of v_d (from reverse to direct bias voltage) the shunt current i_{sh} and the diode current i_d can be deduced as follows:

$$i_{sh} = \frac{V_d}{R_{sh}} \tag{1.21}$$

$$i_d = I_0 \left(\exp\left(\frac{V_d}{nV_T}\right) - 1 \right) \tag{1.22}$$

Once i_{sh} and i_d are calculated, the output current i can be deduced as seen in equation (1.23):

$$i = I_{ph} - i_{sh} - i_d \tag{1.23}$$

After that the output voltage is obtained by a simple subtraction between the diode voltage and the series resistance voltage as reported in equation (1.24):

$$v = v_d - R_s i \tag{1.24}$$

Fig. 1.16 shows the experimental $i-v$ curves compared with those calculated and the related fitting statistical accuracy factor: coefficient of determination R^2 , the Root Mean Squared Error (RMSE), the Mean Bias Error (MBE) and the Mean Absolute Error (MAE) are reported in Table 1.8, respectively. Fig. 1.17 shows the R^2 dependence on R_s and confirms the theory described in Section 1.2.

Table 1.8: *statistical factor obtained with method 2.*

Environmental conditions	$G=0 \text{ Wm}^{-2}, T=27 \text{ }^\circ\text{C}$	$G=345 \text{ Wm}^{-2}, T=36 \text{ }^\circ\text{C}$
R^2	0.9999	0.9999
RMSE	0.0466	0.0497
MBE	-0.0017	0.0124
MAE	0.0279	0.0189

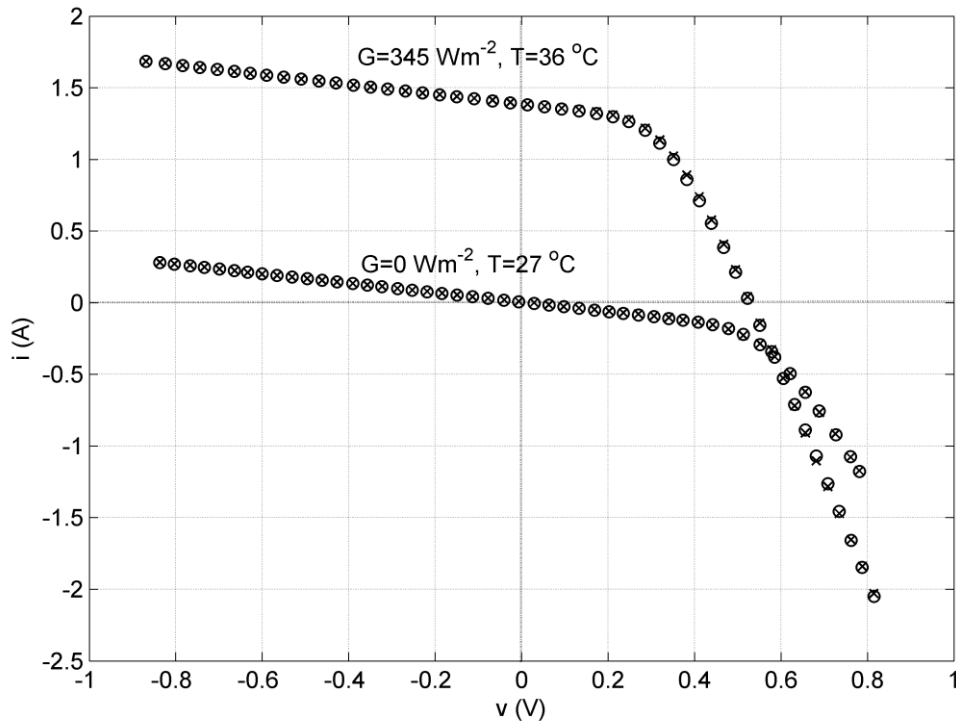


Fig. 1.16 SC output characteristic: experimental ('x' marker) curve and calculated curve ('o' marker) for two different conditions.

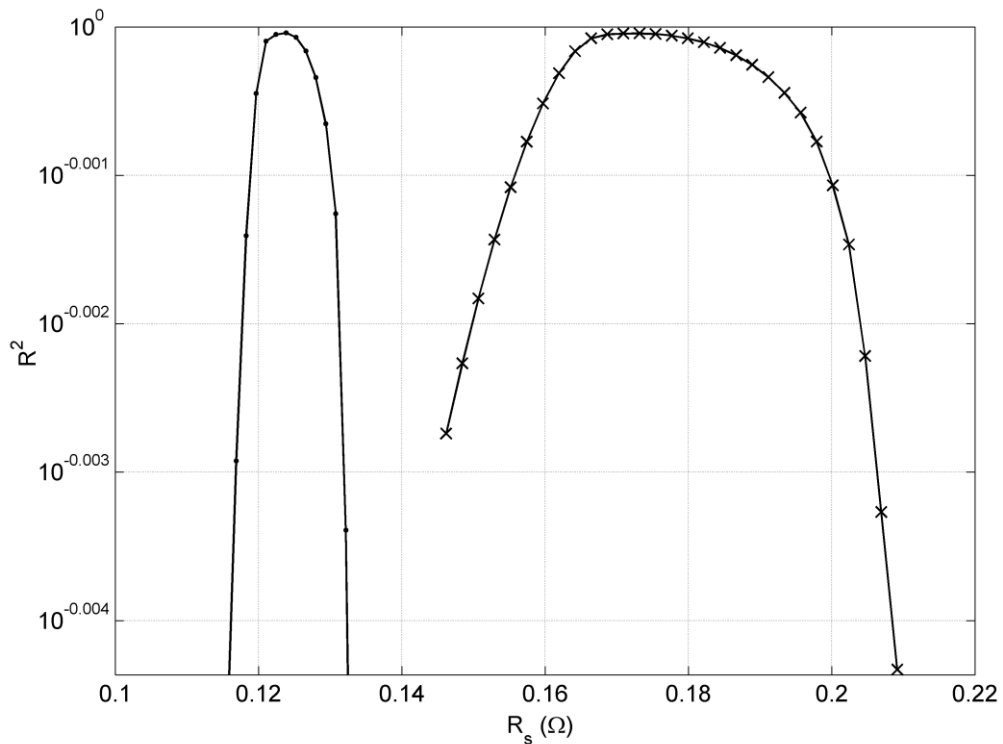
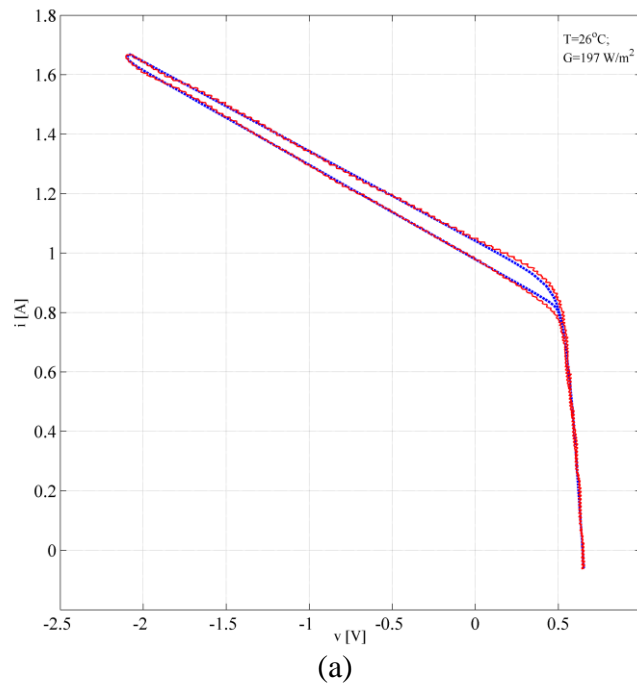


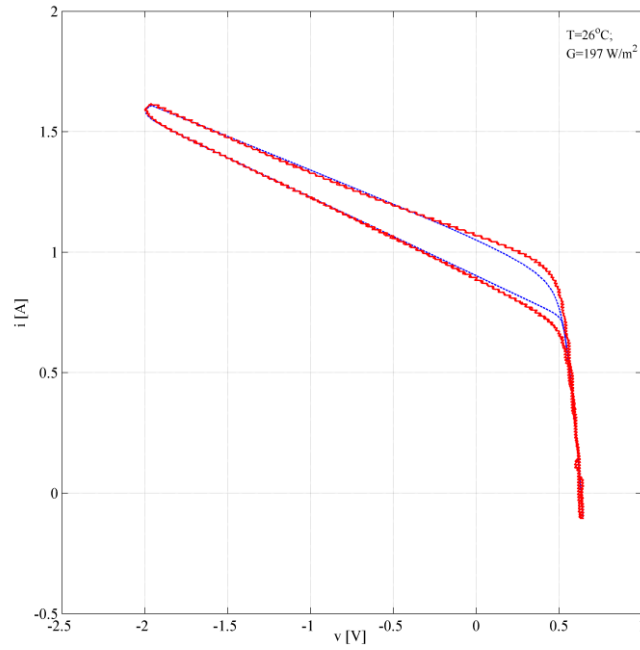
Fig. 1.17 R^2 dependence with R_s , for illuminated (.' marker) and dark ('x' marker) conditions. Lines are a guide for the eye.

1.5.3 Dynamic model

The electrical dynamic model of the SC was designed as an electric circuit in Simscape² suite. I_{ph} is represented by an ideal current generator; the diode model used is an ideal one which reflects the diode function presented in the characteristic equation and take account of I_0 and n ; R_s and R_{sh} are represented by a static resistance and finally the parasitic capacitance is subdivided in two parallel capacitance, as obtained in section 1.4.3 and reported in Table 1.5, where the first one is constant and the second one depends linearly on the output voltage of the SC. Development of this circuital model is straightforward for other environments like PSpice and Cadence. The simulated output characteristics are reported and compared with the experimental results for the two frequency bias 1 kHz and 2.5 kHz as can be seen in Fig. 1.18 (a) and 1.18 (b), respectively. R^2 is calculated for rising bias current ($\partial v/\partial t < 0$) when c_p has a discharge effect and for falling bias current ($\partial v/\partial t > 0$) when c_p has a charge effect. Results are reported in Table 1.9.



² Simscape extends Simulink® with tools for modeling systems spanning electrical and other physical domains...



(b)

Fig 1.18 Experimental (solid line) and simulated (dashed line) output characteristic (a) at 1 kHz (b) at 2.5 kHz

Table 1.9: R^2 obtained for the dynamic model

Conditions	Frequency	R^2
$\partial v / \partial t < 0$	1 kHz	0.9969
$\partial v / \partial t > 0$	1 kHz	0.9954
$\partial v / \partial t < 0$	2.5 kHz	0.9933
$\partial v / \partial t > 0$	2.5 kHz	0.9936

1.6 Environmental model

The electrical behavior of the SC changes with the two environmental parameters irradiance and temperature of the SC. At any given G and T it corresponds an $i-v$ curve which can be replied by the model with proper parameters set. The ability to establish a law to define the dependence of the five electrical parameters on G and T permits the construction of an equivalent environmental model based only on these two parameters. As consequence, this environmental model will accept G and T as input and outputs directly the $i-v$ curve. This model can be helpful to simulate and analyze the mismatch effect of a PV array system as dependence on G and T is straightforward. To obtain an accurate environmental model, it is necessary to analyze a quantity of $i-v$ curves data, for a specific SC, over a wide range of G and T , in order to determine the variation. A specific law will be found which can be adequate for SC of the same kind of the one considered up to the specific constant [31-32]. Finally, the aging factor of SC can be taken in account to complete it. A first investigation using the parameters found through the N-R method to explore their dependency on G and T is reported in this section.

1.6.1 Parameters dependence on G and T

The availability of electrical parameters in a range on G and T (Table 1.1 and 1.2) allows an analysis of the parameters behavior with G and T . The following fitting functions have been applied: I_{ph} depends linearly on G ; I_0 depends on the cubic power of T ; R_s depends on the cubic power on G and T ; R_{sh} can be fitted by a smoothing exponential with G and T . I_{01} and I_{02} depend on the cubic and square power of T , respectively. In Table 1.10, the equation obtained from the fitting is shown with the relative coefficient of determination; X is used when dependence is not determined. Figs. 1.19-1.22 shows the parameters extracted for various environmental conditions as function of G and T , it includes the error bar associated with each parameter (evaluated from statistical analysis performed in Section 1.4.1) and the fitting curve from the physical models. This is a first attempt to built a phenomenological methods based on G and T . To have an accurate fitting, a wide range of measurements has to be performed.

Table 1.10: Parameters fitting equation to G and T with related R^2

parameters	G	R^2	T	R^2
I_{ph} (A)	$0.008326G - 0.04169$	0.9991	X	X
I_0 (A)	X	X	$I_0 = 2.633e-11T^3 - 1.719e-9T^2 + 3.654e-8T - 2.321e-7$	0.665
R_s (Ω)	$3.62e-11G^3 - 7.426e-8G^2 + 4.545e-5G + 0.008429$	0.7204	$1.62e-6T^3 - 1.6e-4T^2 + 0.005059T - 0.03528$	0.8838
R_{sh} (Ω)	$44.29 \exp(-0.003492G)$	0.9258	$134.8 \exp(-0.09178T)$	0.6584
n	X	X	X	X
I_{01} (A)	X	X	$I_{01} = 1.669e-12T^3 - 1.176e-10T^2 + 2.762e-9T - 2.034e-8$	0.9786
I_{02} (A)	X	X	$1.983e-8T^2 - 1e-10$	0.6133

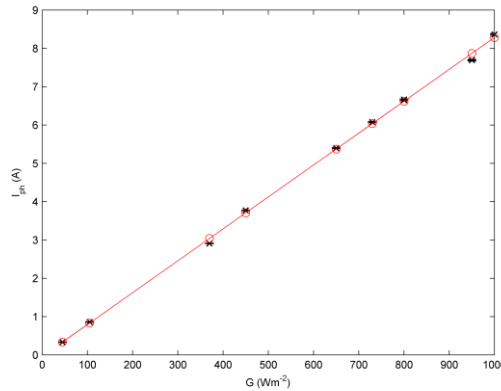


Fig. 1.19 $M-1$, Variation of I_{ph} with G ; 'x' marker is the extracted parameter value with error bars, 'o' marker indicates the fitting points.

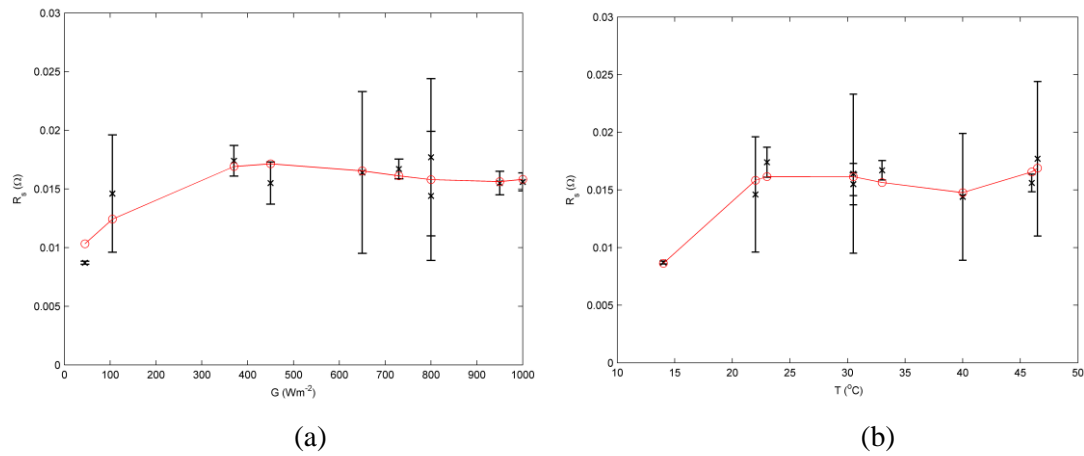


Fig. 1.20 (a) $M-1$, variation of R_s with G , (b) $M-1$, variation of R_s with temperature (T); 'x' marker is the extracted parameter value with error bars, 'o' marker indicates the fitting points.

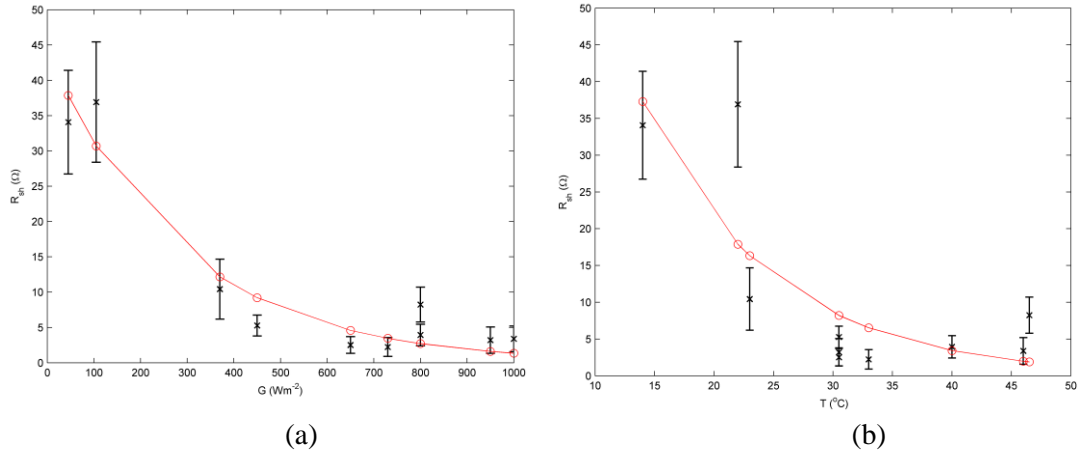


Fig. 1.21 (a) $M-1$, variation of R_{sh} with G , (b) $M-1$, variation of R_{sh} with T ; 'x' is the extracted parameter value with error bars, 'o' marker indicates the fitting points.

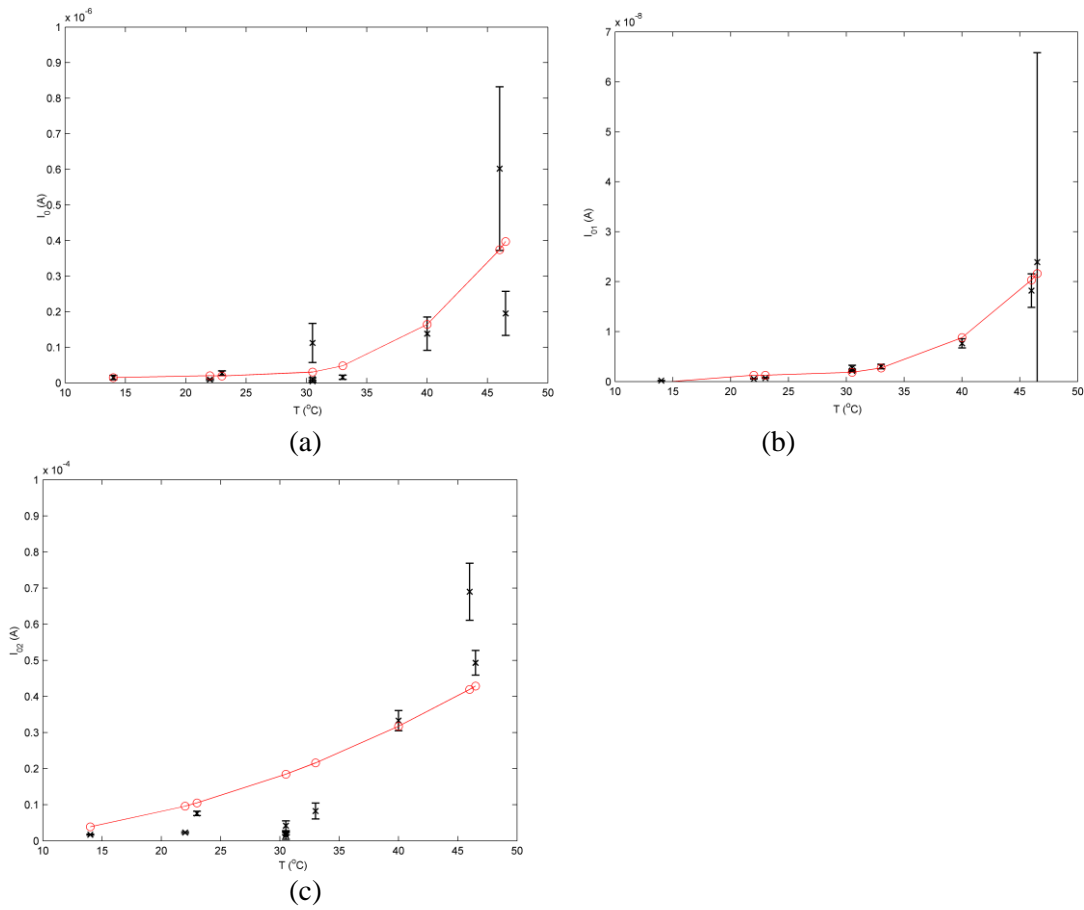


Fig. 1.22 (a) $M-1$, variation of I_0 with T , (b) $M-2$, variation of I_{01} with T , (c) $M-2$, variation of I_{02} with T ; 'x' is the extracted parameter value with error bars, 'o' is the fitting points.

1.7 Mismatch

In solar photovoltaic arrays, SCs are connected in series and parallel in the network to match the required voltage and current requirements. An undesirable and important feature of the solar PV arrays that has emerged from the field experience is that their output power ratings based on name plate rating of modules are universally higher than those observed in field conditions even when the operating conditions were close to standard test conditions (STC). The feature of delivering lower power than the array ratings in the field conditions is often referred to as mismatch loss i.e. variations between solar cell characteristics [33]. The mismatch effect in PV arrays can be due to a variety of reasons [34]:

- Manufacturer's tolerances in sc characteristics: physical differences between SC may arise during normal processing and different SCs may have slightly different characteristic parameters. Consequently, in an array, the output power of the combination is less than the sum of maximum output power of constituents. This power loss may tend to enhance with time due to degradations resulting from aging.
- Environmental stresses: in the field, solar cells arrays are subject to shadowing, temperature gradient, aging, and temperature shock ...The two factors under study are shadow effect and temperature gradient.

1.7.1 Shadow effect

PV solar cells series connected suffer the shadowing because shadowed SC has a large detrimental effect on series voltage as series current is forced by the other SCs and this can cause large reverse bias and consequently hot spots, and eventually, damage or failure [35].

To study the shadow effect and to verify if it is possible to reduce its effect in power loss, a structure of solar cells was built and shown in Fig 1.23. It is composed of four commercial monocrystalline solar cells (125×125 mm) connected in series by a service switch to allow single SC characterization. The electrical data under standard test conditions ($G=1000\text{W/m}^2$, $T=25$ °C, $AM=1.5$) are: P_M , 2.06 W, I_M , 4.33 A, V_M , 0.475 V. Each SC is parallel connected with a series of a switch and a bypass diode.

The electrical schematic of the structure is shown in Fig. 1.24 (a). The four SCs are labeled from the left to the right by A, B, C and D and their output voltage are indicated by V_A , V_B , V_C , and V_D respectively. The bypass diodes are called D_A , D_B ,

D_C , and D_D . The switches connected in series with the bypass diodes are named SW_A , SW_B , SW_C and SW_D . The output current and voltage of the whole system are denoted by i and v respectively. The standard solar panel is represented when SW_A , SW_B , SW_C and SW_D are open and this configuration is called PV_1 , Fig. 1.24 (b). When all these switches are closed, each SC presents a bypass diode, and this configuration is nominated PV_2 (Fig. 1.24 (c)). Series resistances of the switches are two orders of magnitude lower than SC series resistance; therefore they do not affect the study in exam. The measurements were done inside laboratory and two halogen lamps of 500 W were used. Light was evenly distributed between the four SCs. The height of the lamp can be modified manually to choose the desired illumination which is measured by a Mac-Solar radiation meter. To characterize the solar panel, a set of fixed resistor was built to load the panel solar or the SCs in different working points and presents different values (0.106, 0.223, 0.333, 0.474, 0.697, 1.008, 1.334, 2.211, 3.328, 4.976, 10.067, 15.507, 22.429, ∞) $\pm 0.001 \Omega$. The temperature is detected by a thermocouple. Two ventilators were used to maintain constant the temperature of SCs between $\pm 2^\circ \text{C}$ for any measurement condition; this is to reduce the mismatch caused only by the shadowing effect and manufacture tolerance. The voltage and the current in exam are measured by 'keithley' digital multimeters. The shadowing effect is performed by partial obscuration of chosen SC by a thick opaque pad.

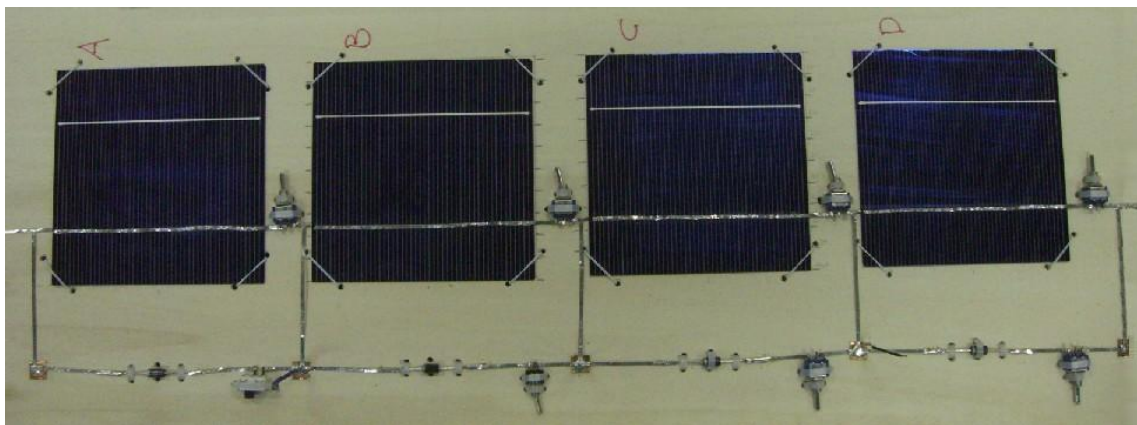


Fig. 1.23 The structure built for four series SC; each SC is parallel connected with a series of a switch and a bypass diode.

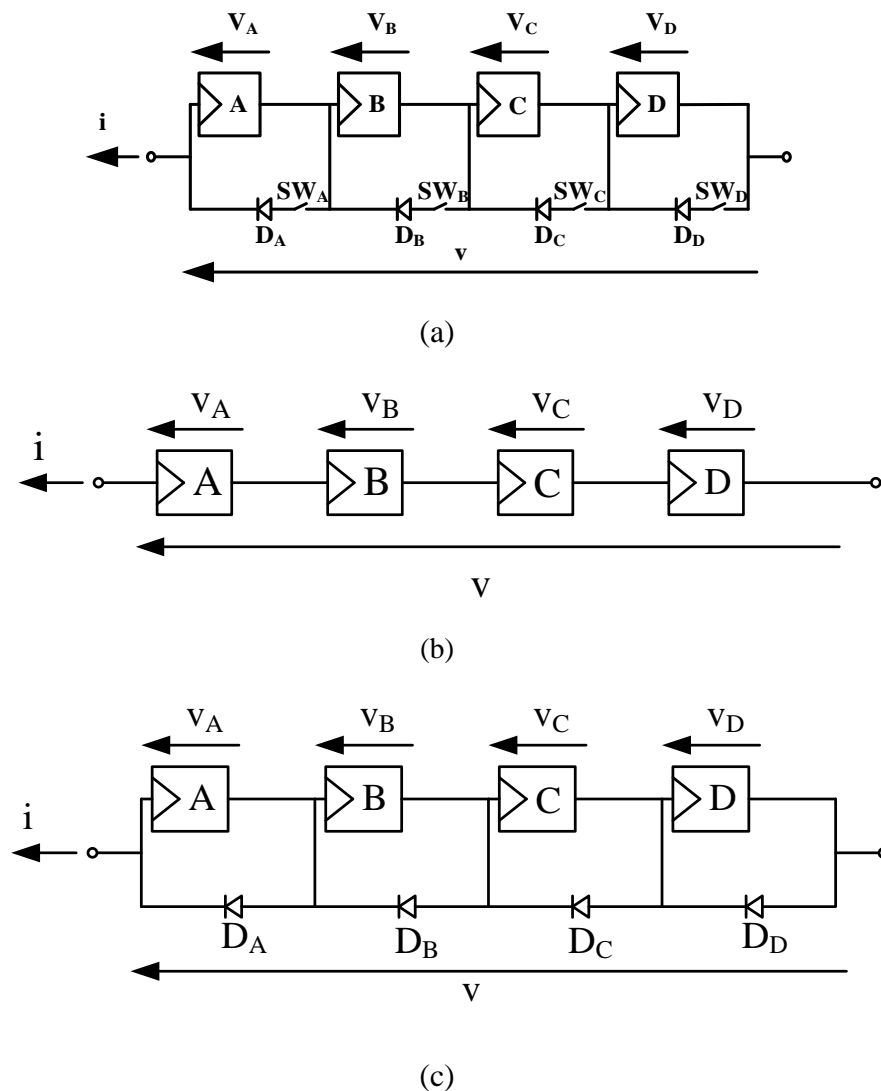


Fig. 1.24 (a) The circuit schematic of the built structure. (b) The standard solar panel configuration PV₁. (c) The modified solar panel configuration PV₂ a bypass diode is added in parallel of each SC.

The shadowing effects have been verified with six tests. The SC named ‘C’ was obscured from 0 up to 100 % of its area and each test was performed in the same climatic conditions. PV₁ and PV₂ configurations have been contextually characterized by manual operation of switches. Output power results and analysis are reported and discussed in the following:

The first test was done to verify that SC acts in a first line in the same manner. After that, the following problem is addressed: the SC named ‘C’ is obscured of 0 %, 30 %, 60 %, 80 % and 100 %, respectively. In each case and at the same climatic conditions the characterization in power terms of the whole system was done for both PV₁ (standard solar panel) and PV₂. Results and analysis are reported and discussed in the

following:

- Test 0 %: SC 'C' is not obscured; all the SC acts as a generator. The bypass diodes in PV₂ configuration are reverse biased and the same amount of output power for both PV₁ and PV₂ configuration is expected. Results are shown in Fig. 1.25 where the two curves are similar, considering measurements errors. The maximum power generated by PV₁ and PV₂ configurations is very close 1999.65 mW and 1996.88 mW respectively.

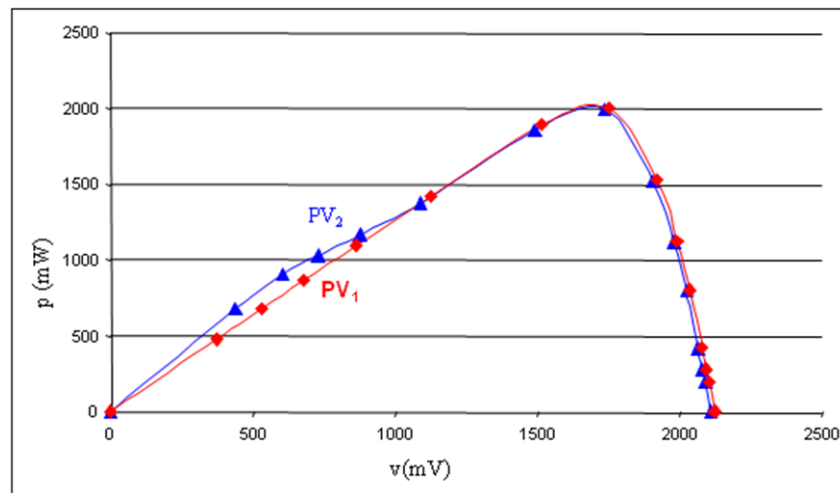


Fig. 1.25 Output power for PV₁ and PV₂ configurations with C obscured by 0 % at the same conditions.

- Test 30 %: C area obscured by 30 %; the maximum power generated by PV₁ is 1847.76 mW while that generated by PV₂ is 1806.93 mW. The power output characteristic is shown in Fig. 1.26 for both systems.

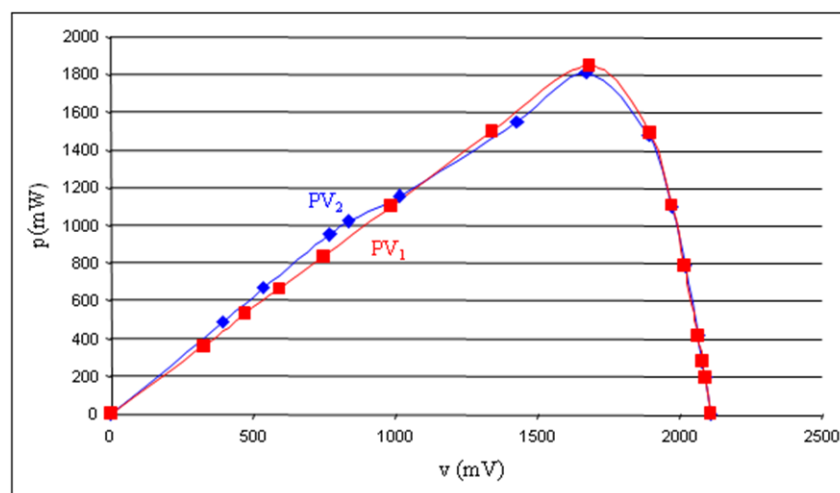


Fig. 1.26 Output power for PV₁ and PV₂ configurations with C obscured by 30 % at the same conditions.

- Test 60 %: C obscured by 60 %. In Fig. 1.27, we can see the two configurations deliver different results. PV_1 shows a traditional curve while PV_2 configuration presents two maximum power points. This effect can be explained by a circuit analysis. For low bias voltage, the introduction of the bypass diodes allows the clear SC current to have a path to flow when SC 'C' is reverse biased (Fig. 1.28 (a)). For voltage higher than 1000 mV, also 'C' is forward biased; the bypass diode is shut down and the curve close back to PV_1 (Fig. 1.28 (b)). The low voltage MPP is due to the series of the elements A, B, D_C , and D while the high voltage one is due to A, B, C, and D. The absolute MPP of PV_2 configuration is obtained with the bypass diode conducting, and it is 1078.16 mW. The MPP obtained from the PV_1 configuration is 1038.2 mW.

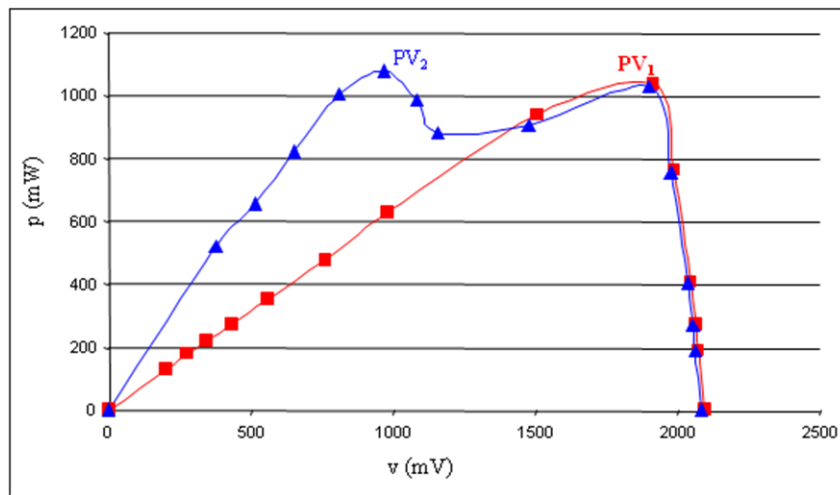


Fig. 1.27 Output power for PV_1 and PV_2 configurations with C obscured by 60 % at the same conditions.

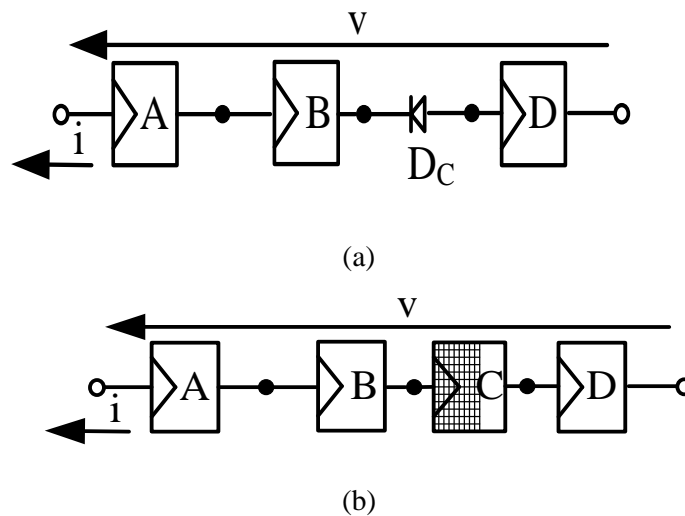


Fig. 1.28 (a) Ideal equivalent circuit schematic at low bias voltage for PV_2 configuration with SC 'C' obscured by 60 %. (b) Ideal equivalent circuit schematic at high bias voltage for PV_2 configuration with SC 'C' obscured by 60 %.

- Test 80%: C obscured by 80 %; previous situation is exalted and the absolute MPP in PV₂ configuration (1059.5 mW) is much higher than the MPP in PV₁ configuration (562.99 mW), results are reported in Fig. 1.29.

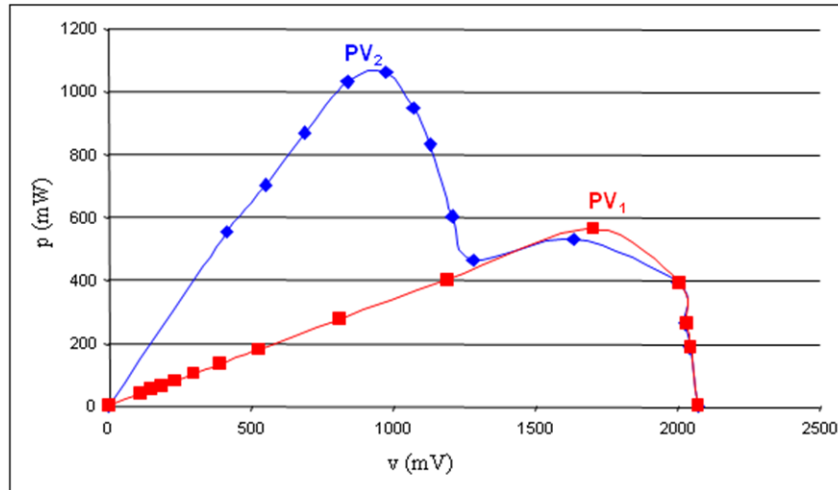


Fig. 1.29 Output power for PV₁ and PV₂ configurations with C obscured by 80 % at the same conditions.

- Test 100%: C is totally obscured; there is not a path for the current in PV₁ configuration as the SC 'C' acts as an open circuit in this situation; the output power is zero. While for PV₂ configuration, the output power amount is due to the series of the elements A, B, D_C and D and results equals to 1018 mW. For low voltage p - v curve of PV₂ configuration remain constant.

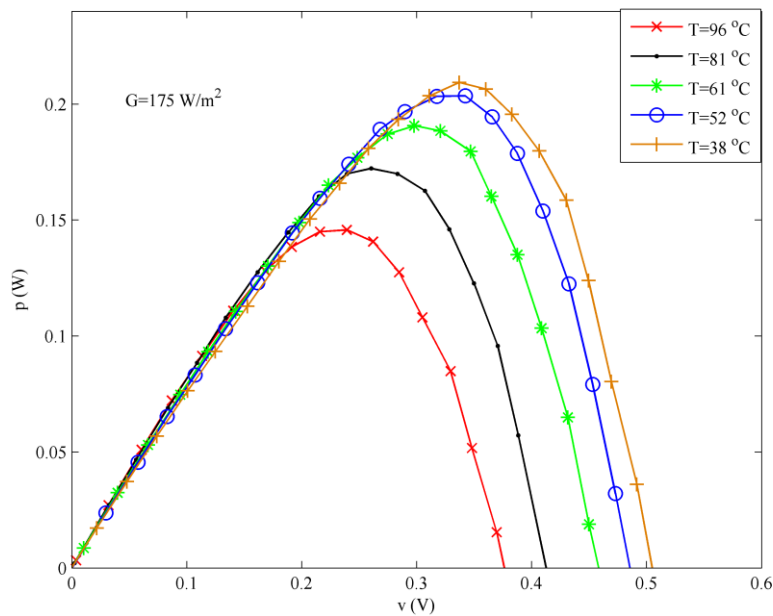
A summary of the results obtained is reported in Table 1.11. The first column reports the degree of obscuring of SC 'C'; the second column reports the maximum power point in PV₁ (MPP₁) configuration; the third column reports the maximum absolute power point in PV₂ (MPP₂) configuration and the last column reports the ration between MPP₂ and MPP₁.

Table 1.11 Summary of the results

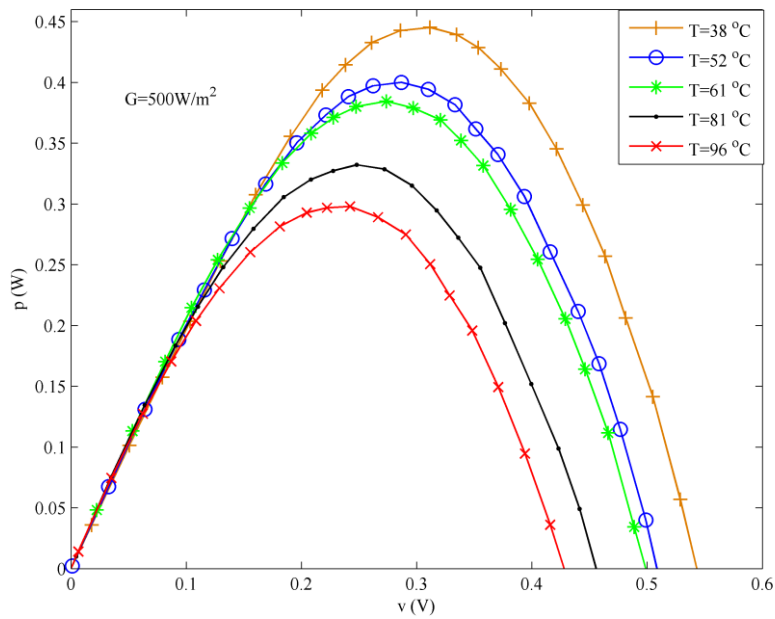
% obscuring of 'C' @ G=350W/m ² , T=38 °C	MPP ₁ (mW)	MPP ₂ (mW)	MPP ₂ /MPP ₁
0	1999.65	1996.88	0.999
30	1847.76	1806.93	0.978
60	1038.2	1078.16	1.04
80	562.99	1059.5	1.882
100	0	1018	∞

1.7.2 Temperature effects

In the field, the distribution of the temperature is not uniform under the same panel; each SC presents a different working temperature from the others. This mismatch is not negligible as results of 5 °C can be detected between SCs in the same panel. To check the SC in different working points maintaining temperature under control, the measurement setup reported in a previous section to highlight the capacitance is used. This test allows quasi-static temperature measurement (< 0.1 s). Ten distinct measurements are done using the same commercial monocrystalline SC at five different temperatures and at two levels of irradiance. The output power characteristics obtained are shown in Fig. 1.30 (a) and Fig. 1.30 (b) for $G=175$ W/m² and $G= 500$ W/m² respectively. A difference between the output characteristics at the same level of irradiance due to the mismatch of the working temperature of the SC can be noted. The maximum power point obtained for each temperature is shown in Fig. 1.31. The maximum output power decreases as temperature at a fixed irradiation increases. A variation of maximum power equals to 0.064 mW and 0.25 mW due to a variation of temperature of 58 °C (96-38) is obtained at $G=175$ W/m² and $G=500$ W/m² respectively. Power loss is approximately 0.5%/°C.



(a)



(b)

Fig. 1.30 Output power characteristic vs output voltage for a SC (a) $G=175 \text{ W/m}^2$ (b) $G=500 \text{ W/m}^2$; ($T=38 \text{ }^\circ\text{C}$ ‘÷ marker’, $T=52 \text{ }^\circ\text{C}$ ‘o marker’, $T=61 \text{ }^\circ\text{C}$ ‘* marker’, $T=81 \text{ }^\circ\text{C}$ ‘· marker’, $T=96 \text{ }^\circ\text{C}$ ‘x marker’).

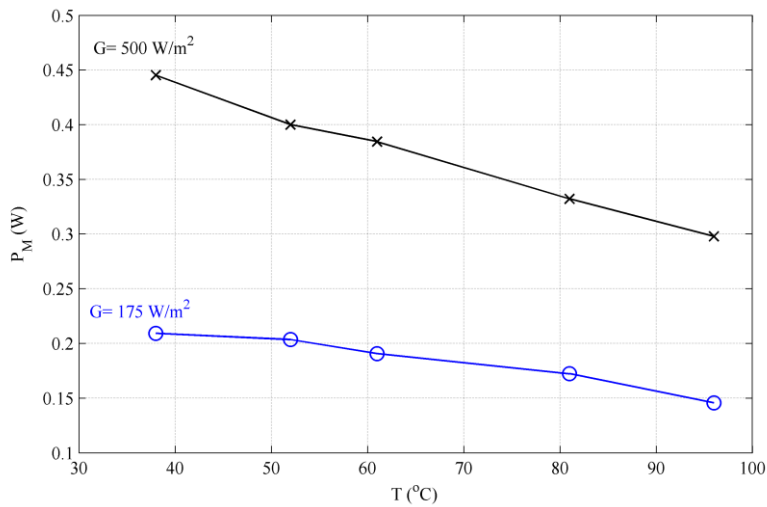


Fig. 1.31 Maximum output power vs the operating temperature of SC for the measurements effected.

1.7.3 Considerations

Small mismatch leads to efficiency losses because the worst SC conditions compromise the output of all the other SCs connected in the series array. Large mismatch can lead to failure, and this is usually dealt through the introduction of some diodes to limit inverse voltage and dissipated power in the worst SC. For these reasons, there is an interest in distributed control of the MPPT down to the smallest element.

1.8 Conclusion

Model parameters for single and dual diode model have been developed using different techniques. The choice of calculating all the parameters without idealization or simplification leads to a good accuracy. N-R method has some convergence problem which is attenuated with the introduction of an exponential factor. It is easy to be used and solves the problem in split seconds. Using this technique, parameterization in G and T using fitting functions has been proposed. The SVO method is an original approach which is independent of the optimization method, fast, very accurate and extremely robust. It presents no convergence or stability problem and solution is delivered in fraction of seconds on desktop computer. The dynamic model is investigated highlighting the effect of the parasitic capacitance. The effect of the capacitance is evidenced and examined analytically through the dynamic model of the solar cell. The splitting of the output characteristic of SC is justified by the presence of this capacitance when it is characterized with high frequency bias. A linear dependence of this capacitance with the output voltage was found. Finally, the mismatch effects have been studied both for darkening and temperature.

Chapter 2

MAXIMUM POWER POINT TRACKERS

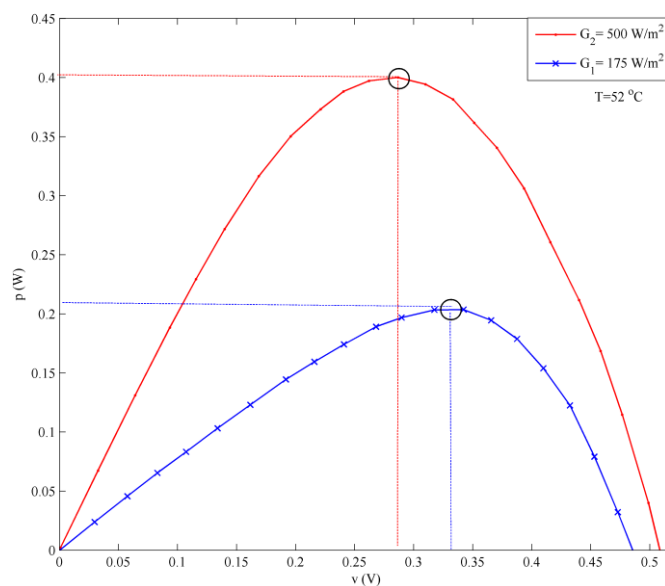
In this chapter, a review of the maximum power point tracking (MPPT) algorithms for photovoltaic systems is reported. The dynamic effects of SC response to a capacitive load are discussed. A novel technique derived from this consideration is proposed which collects the main advantages of the most used algorithms.

2.1 Introduction

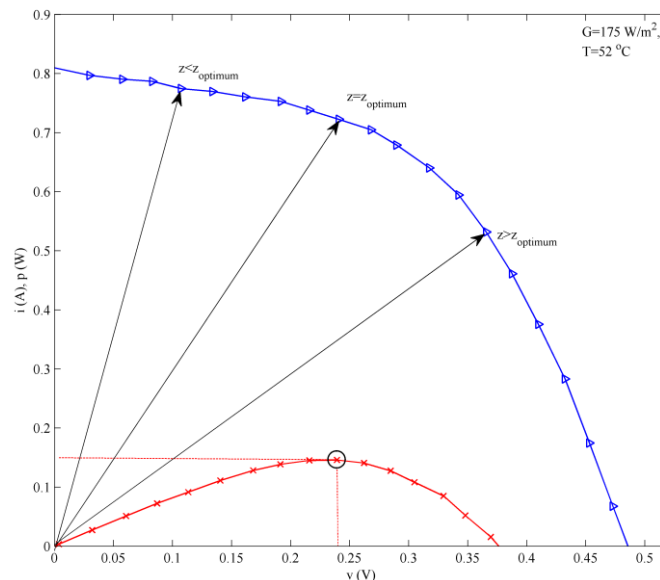
The photovoltaic (PV) generator exhibits a non linear $i-v$ characteristic and its output power depends strongly on three factors [6]: irradiance (G), solar cell temperature (T) and load profile (z, load impedance). Therefore, there is optimum load impedance for the PV generator which corresponds the maximum output power. An example for each factor G, T and z that affects the MPP is reported in Fig 2.1 (a), Fig. 2.1 (b) and Fig. 2.1 (c) respectively. It is evident that when there is a generic request for maximum output power delivery from the PV generator, it is important that the impedance of the PV generator to be near or equals to the optimum load impedance. This can be performed decoupling the actual load from the PV generator by an intermediate DC-DC converter controlled by the so called Maximum Power Point Trackers (MPPT) algorithms. It permits to use the PV system efficiently in all conditions. General MPPT algorithms have been investigated in literature. Among the many classifications that have been proposed, we find that the division in direct (true seeks) and indirect (quasi seeks) methods in [36] is particularly representative of the MPPT nature. The indirect methods are based on a mathematical approximation of a specific PV generator. Therefore, a need for a prior characterization is necessary and actual MPP is estimated from the measure of voltage or current of the PV generator, irradiance, temperature or other empirical data. Therefore, there is no general and not

even an exact way to obtain the MPP for every environment condition. Furthermore, they are prone to long term deviation of actual PV generator characteristics from the initial data set condition (aging effects).

The direct methods offer the advantage to obtain the actual maximum power from continuous measurements of voltage or current of the PV generator. Given the output power curve shape, these algorithms are general and insensitive to environment conditions and long term deviation. Actually, these methods perform ringing around the MPP limited by algorithm step size and system resolution. They are suitable for any irradiance and temperature.



(a)



(b)

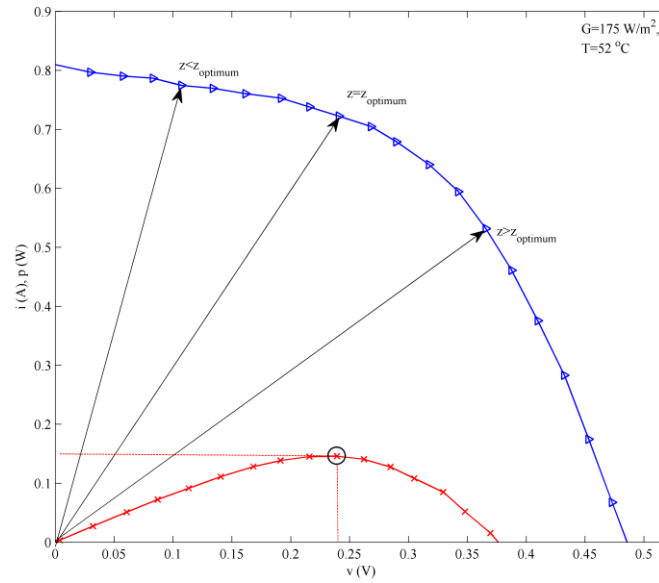


Fig. 2.1 MPP depending on the three main factors; (a) depending on G ; (b) depending on T ; (c) depending on the load

In [37], a brief discussion and categorization of all the main methods is carried out based on: their implementation, the sensors required, their ability to detect multiple local maxima, their costs and applications they suit. A summary of the major characteristics of these methods is reported in Table 2.1. A theoretical assessment of MPPT with different converter topologies is analyzed. After that, the most used MPPTs are described. A novel method based on a single voltage sensor which employs a bridge capacitor structure to extract the maximum power available from PV sources is presented analytically, by simulation and experimentally.

Table 2.1: Major characteristics of MPPT techniques [37].

MPPT Technique	PV Array Dependent?	True MPPT?	Analog or Digital?	Periodic Tuning?	Convergence Speed	Implementation Complexity	Sensed Parameters
Hill-climbing/P&O	No	Yes	Both	No	Varies	Low	Voltage, Current
IncCond	No	Yes	Digital	No	Varies	Medium	Voltage, Current
Fractional V_{OC}	Yes	No	Both	Yes	Medium	Low	Voltage
Fractional I_{SC}	Yes	No	Both	Yes	Medium	Medium	Current
Fuzzy Logic Control	Yes	Yes	Digital	Yes	Fast	High	Varies
Neural Network	Yes	Yes	Digital	Yes	Fast	High	Varies
RCC	No	Yes	Analog	No	Fast	Low	Voltage, Current
Current Sweep	Yes	Yes	Digital	Yes	Slow	High	Voltage, Current
DC Link Capacitor Droop Control	No	No	Both	No	Medium	Low	Voltage
Load I or V Maximization	No	No	Analog	No	Fast	Low	Voltage, Current
dP/dV or dP/dI Feedback Control	No	Yes	Digital	No	Fast	Medium	Voltage, Current
Array Reconfiguration	Yes	No	Digital	Yes	Slow	High	Voltage, Current
Linear Current Control	Yes	No	Digital	Yes	Fast	Medium	Irradiance
I_{MPP} & V_{MPP} Computation	Yes	Yes	Digital	Yes	N/A	Medium	Irradiance, Temperature
State-based MPPT	Yes	Yes	Both	Yes	Fast	High	Voltage, Current
OCC MPPT	Yes	No	Both	Yes	Fast	Medium	Current
BFV	Yes	No	Both	Yes	N/A	Low	None
LRCM	Yes	No	Digital	No	N/A	High	Voltage, Current
Slide Control	No	Yes	Digital	No	Fast	Medium	Voltage, Current

2.2 Converter topologies for MPPT

DC-DC converters are widely used in photovoltaic power systems as an interface between the PV generator and the load, allowing the follow-up of the MPP. Its main task is to condition the power generated by the PV generator, following a specific control strategy by continuously adjusting its voltage and current. The input impedance of the DC-DC converters shows dependence on a number of parameters such as load impedance, duty cycle (governed electronically using an appropriate MPPT strategy), etc... Depending on the type of the DC-DC converter topology used, different matches between input and output impedance can be realized, which significantly affects the PV system's performance [38-39]. Mathematical analysis for the three basic DC-DC converters topologies are addressed regarding their operating requirements such as the minimum and maximum value of the load to be connected to the converter. The assumptions used in the analysis are: switching elements are ideal, passive components are linear, fixed load (R), time-invariant and frequency-independent.

Fig. 2.2 shows the diagram of a PV generator connected to a DC-DC converter; where V and I are the average voltage and current of the PV generator respectively; V_0 , I_0 are the output voltage and current of the load respectively. Fig. 2.2 (a), (b), and (c) show the three basic DC-DC converters topology buck, boost, buck-boost, respectively.

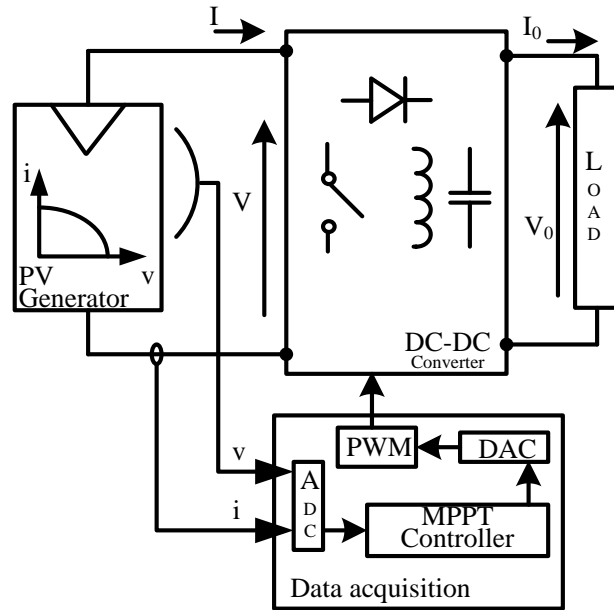


Fig. 2.2 Block diagram of the DC-DC converter controlled MPPT system

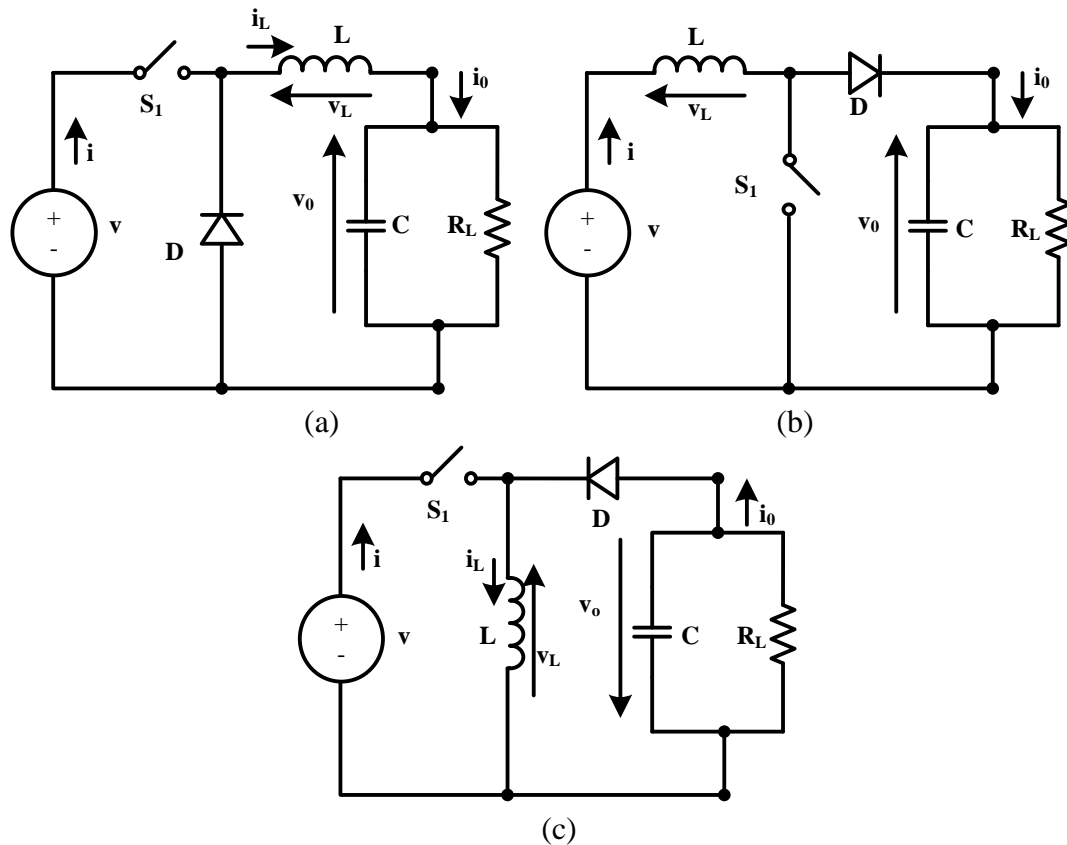


Fig. 2.3 Three basis converter topologies; (a) Buck; (b) Boost; (c) Buck-Boost

2.2.2 Theoretic analysis

The analysis in this paragraph is referred to the buck converter circuit, reported in Fig. 2.3 (a), and deduction of the results for the other two converters is straightforward. The following mathematical relationships can easily be established:

$$V = \frac{V_0}{D} \quad (2.1)$$

$$I = \frac{I_0 D}{\eta} \quad (2.2)$$

where η is the efficiency of the converter. The above equations are obtained based on voltage gain of the converter and the efficiency definition ($V_0 I_0 = \eta V I$). From equations (2.1) and (2.2) the equivalent load R_{eq} , due to a combination of DC-DC converter and a fixed load R , appearing across the PV generator terminals can be written as:

$$R_{eq} = \frac{V}{I} = \frac{\eta R}{D^2} \quad (2.3)$$

The above expression gives the effective load across the PV generator terminals, which can be smoothly controlled over wide ranges using duty ratio. From equation (2.3), the optimum duty cycle D_M corresponding to the MPP when R_{eq} is equal to V_M/I_M and noted by R_M is carried out:

$$D_M = \sqrt{\eta \frac{R}{R_M}} \quad (2.4)$$

The operating range of the duty cycle should be D_{min} to D_{max} , and consequently, the optimum duty cycle D_M belongs this interval:

$$D_{min} < D_M < D_{max} \quad (2.5)$$

From equation (2.4) and from the interval of variation of the duty cycle, the value range of the load R is deduced:

$$\frac{D_{min} R_M}{\eta} < R < \frac{D_{max} R_M}{\eta} \quad (2.6)$$

The practical range of the duty cycle is approximately 0.1 to 0.9 for D_{min} and D_{max} , respectively and the efficiency is about 90%. For these values the approximate load range is:

$$0.0011 R_M < R < 0.9 R_M \quad (2.7)$$

The last inequalities should be satisfied for all possible values of R_M for a specific PV generator. If the value of R does not satisfy these inequalities, a ‘MPP non capture zone’ is created for DC-DC buck converter as shown in Fig. 2.4. The ‘MPP non capture zone’ is found doing the limit of R_{eq} in equation (2.3) when the duty cycle

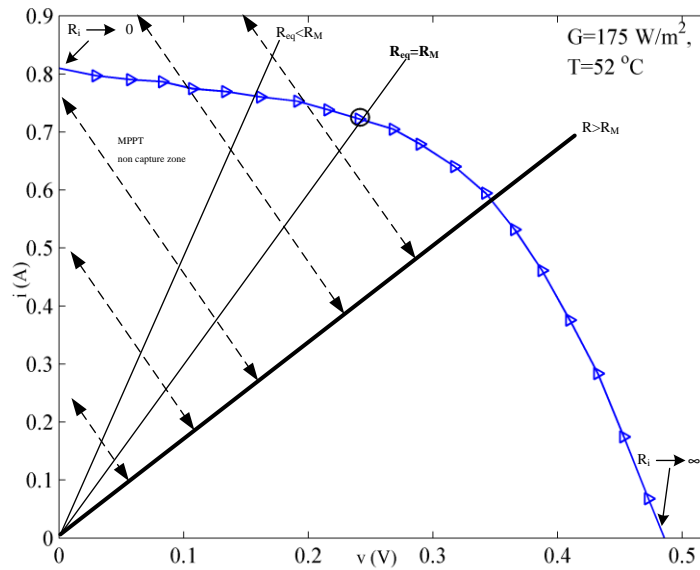


Fig. 2.4 Chart of MPP tracking with buck DC-DC converter. The 'MPP non capture zone' is indicated with shadowed line ($R > R_M$).

tends to 0 and 1. The result is that R_{eq} belongs $[R, \infty)$. If the value of R_{eq} at the maximum power point (R_M) does not belong to the set of values allowed for R_{eq} , the capture of MPP will not be possible. The same analysis is done in [38] for boost and buck-boost converter. The value of R_{eq} in both conditions (continuous and discontinuous conduction mode) belongs to $[0, R]$ for the boost converter and to $[0, \infty)$ for the buck-boost converter. From the analysis developed in this section, the importance of the correct choice of the DC-DC converter in a given application is carried out. To use the system efficiently, it is better to employ a buck-boost converter when a wide variable impedance load is considered and to use a buck or boost when fixed impedance load is considered.

2.3 MPPT

PV systems should be designed to operate at their maximum output power levels for any temperature, solar irradiation level and load impedance at all times. Maximum power point trackers (MPPTs) algorithms are used to track the peak output power of the solar photovoltaic systems (as anticipated in the introduction). The different techniques found in literature can be subdivided in distinct categories and basically in indirect and direct methods. Curve-fitting, look-up table, open-voltage PV generator, short circuit PV generator, etc... belong to the quasi seeking technique, while the perturb and observe (P&O) and the incremental conductance (INC) methods, etc... belong to the true seeking technique.

2.3.1 The indirect methods

In the indirect methods, a prior evaluation of the PV generator is required. It is based on the use of a database that includes parameters and data such as, for instance, typical curves of the PV generator for different irradiances and temperatures, or on the use of the mathematical functions obtained from empirical data to estimate the MPP.

2.3.1.1 Curve-fitting

The output characteristic of a PV generator can be modeled from the conventional single diode model as seen in chapter 1. At a given climatic condition, the optimum voltage doesn't have a direct solution due to the fact that the output characteristic of the PV is implicit. A good approximation near the MPP can be obtained through a polynomial of the third order [40-41] where the output power p can be explicated directly as a function of the output voltage v , as seen in equation 2.8:

$$p = av^3 + bv^2 + cv + d; v \in [V_M - \varepsilon, V_M + \varepsilon] \quad (2.8)$$

where ε is small number and a , b , c and d are coefficients determined by the sampling of m values of PV voltage v and PV current i in the required interval.

Knowing that at MPP the derivative of the output power p respect to the output voltage v is zero, the following results of the MPP is obtained in equation 2.9:

$$V_M = -\frac{b}{3a} \sqrt{b^2 - 3ac} \quad (2.9)$$

To find a fine value of the voltage near the MPP voltage, this process should be repeated with timing compatible with transitory effects (around 10 ms). This method requires accurate knowledge of the physical parameters relating to the solar cell material (a , b , c) and the mathematical expressions used are not valid for all climatic conditions. In addition, it might require a large memory capacity for calculation of the mathematical formulations.

2.3.1.2 Look-up table method

The measured values of the PV generator's voltage and current are compared with those stored in the control system, which correspond to the operation in the MPP [42], under concrete climatic conditions. This algorithm requires a large capacity of memory and presents the disadvantage that the implementation must be adjusted for a specific panel. Moreover, it is difficult to record and store all possible system conditions when the operating temperature and irradiance can present a wide range of operation $[-10\text{ }^{\circ}\text{C}, 80\text{ }^{\circ}\text{C}]$ and $[0\text{ W/m}^2, 1000\text{ W/m}^2]$, respectively. Also, the aging effect should be taken into account; it is a factor which is difficult to establish and it isn't yet discussed in the literature. Another application of the look-up table regards the storage of set of (G, T) conditions; which increases the system complexity with the introduction of G and T sensors.

2.3.1.2 Open-circuit voltage

This algorithm is based on the fact that the MPP voltage V_M is approximately linearly proportional to the open-circuit voltage V_{oc} [43-44] as reported in equation 2.10:

$$V_M \cong k_1 V_{oc} \quad (2.10)$$

k_1 is the proportional coefficient and mainly depends on the fabrication technologies of solar cells and from the meteorological conditions (G and T). In a first approximation, k_1 can be treated as constant for a given solar panel and its range belongs $[0.73, 0.8]$. A dependency of k_1 on G can be found, which makes this method more accurate at the expense of loss of simplicity.

The property reported in equation 2.10 can be implemented by means of the flow chart shown in Fig. 2.5. The open circuit voltage is measured by interrupting the normal operation of the system with a certain frequency. Then, the V_M is deduced using equation (2.10) and the operation voltage is adjusted to the MPP. This process will be repeated periodically as a typical interval of sampling (several tens of ms).

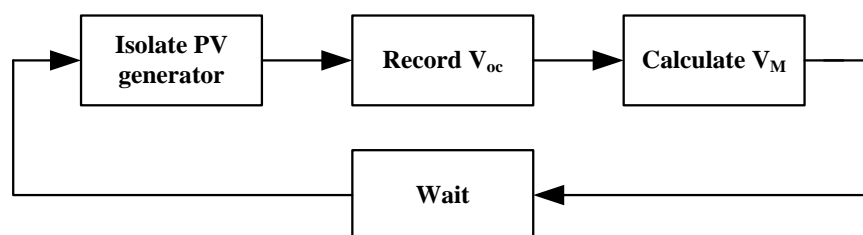


Fig. 2.5 Algorithm flowchart of the open-circuit voltage.

This method appears to be simple, and it is used in micro-system solar cells; where low dissipation power of the control block is mandatory. It is not a true MPPT method as the calculated MPP never matches the real value one. Moreover, the system should be constantly shut down for considerable time to calculate the value of V_{oc} and induce significant power losses. This last problem can be avoided by using a solar cell pilot [45]. In this case, the approximation of the property is less accurate due to mismatch between solar cells and the algorithm failure in case of shadowed conditions.

2.3.1.3 Short-circuit current

This method is similar to the open-voltage circuit one. It is based on the fact that the current at MPP I_M is proportional to short-circuit current I_{sc} [46] as shown in equation 2.11:

$$I_M \cong k_2 I_{sc} \quad (2.11)$$

The proportional coefficient k_2 is a function on the climatic factor G and T and depends on the fabrication technologies. However k_2 assumes a fixed value for a given application, e.g. k_2 is around 0.85 for polycrystalline, and generally it is in the range [0.75, 0.9].

2.3.1.4 Model parameters

The expression of the output power p from a PV generator can be expressed, through the single diode model developed in chapter 1, as a function on temperature of SC, irradiance, and the five electrical parameters. The mathematical equation is reported in 2.12:

$$p = vI_{ph} - vI_0 \left(\exp\left(\frac{v^2 + R_s p}{nV_t v}\right) - 1 \right) - \frac{v^2 + R_s p}{R_{sh}} \quad (2.12)$$

The implicit nature of this kind of equation does not allow a closed solution for a voltage working point, and particularly for the MPP. However, a useful equation can be obtained that presents all possible locations for the MPP current I_M within a range of irradiance and with a fixed temperature. At MPP, the derivative of the output power respect to the voltage is zero and equation 2.13 is obtained from 2.12 as follows:

$$0 = I_{ph} - I_0 \left(\exp\left(\frac{V_M + R_s I_M}{nV_t}\right) \left(1 + \frac{V_M + R_s I_M}{nV_t}\right) - 2 \right) \frac{V_M}{R_{sh}} + I_0 \quad (2.13)$$

Using equation 1.1 in the MPP, the equation 2.14 is obtained:

$$I_M = I_{ph} - I_0 \left(\exp\left(\frac{V_M + R_s I_M}{nV_t}\right) - 1 \right) - \frac{V_M + R_s I_M}{R_{sh}} \quad (2.14)$$

The subtraction of (2.13) from (2.14) permits the elimination of the photocurrent terms, which accounts for the irradiance level, and gives equation (2.15):

$$I_M = \frac{I_0 V_M}{nV_t} \left(1 - \frac{R_s I_M}{V_M}\right) \exp\left(\frac{V_M + R_s I_M}{nV_t}\right) + \frac{2V_M}{R_{sh}} - \frac{V_M + R_s I_M}{R_{sh}} \quad (2.15)$$

From equation 2.15, it is deduced that I_M is a function of V_M , I_M , electric parameters and temperature (being $I_0(T)$ and $V_t(T)$). This function describes all possible locations of the MPP at a fixed temperature. Therefore, the MPP location can be obtained by the intersection between the actual output characteristic of the PV generator at a given climatic conditions and equation (2.15).

This method is developed in [47]; it is shown that the method delivers a convergence speed to MPP higher than the standard method (P&O). It assumes a constant set of the electrical parameters of the model, and this causes large error, as parameters crucially vary with G and T . It is an error mode when the parameters vary with G and T . A high accuracy can be obtained by the implementation of an algorithm for real time parameters evaluation [28]; that makes this method much slower and far more complex.

2.3.2 The direct methods

The true seeking methods include those methods that use PV voltage or current measurements. From those measurements and the information of the variations of the PV generator operating points; the location of the optimum operating point is obtained. These algorithms have the advantage of being independent from the a priori knowledge of the PV generator characteristics. Thus, the operating point tracking is independent of irradiance, temperature or degradation levels. The problems are measurement errors and step size which strongly affect tracker accuracy and response time to environment changes. The methods belonging to this group basically include the Perturb and Observe (P&O) and the Incremental Conductance (INC).

2.3.2.1 Perturb and Observe

The ‘P&O’ is the most commonly used by the majority of authors, and at present, is the industry standard [48-51]. It is an iterative method based on the measures of the PV generator characteristics voltage and current. The basic idea of this method is shown graphically in Fig. 2.6 and the associated flowchart algorithm is shown in Fig. 2.7. Fig. 2.8 shows a possible implementation of the P&O. The operating voltage v is perturbed by a small increment Δv and the resulting change in power Δp is calculated.

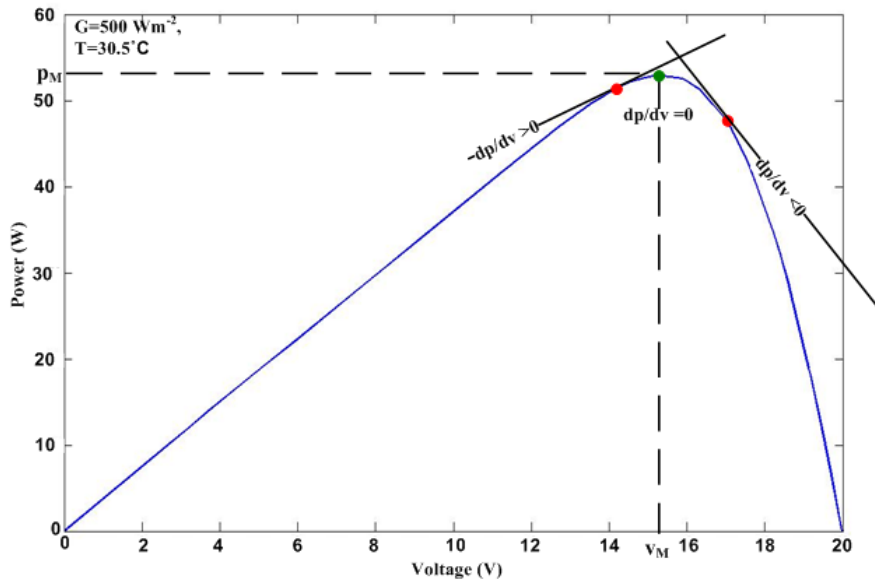


Fig. 2.6 The variation of the output power gives the information of the location of the MPP ($dp/dv < 0$ indicates that the operating point is at the left on the MPP; $dp/dv > 0$ at the right on the MPP; $dp/dv = 0$ at the MPP)

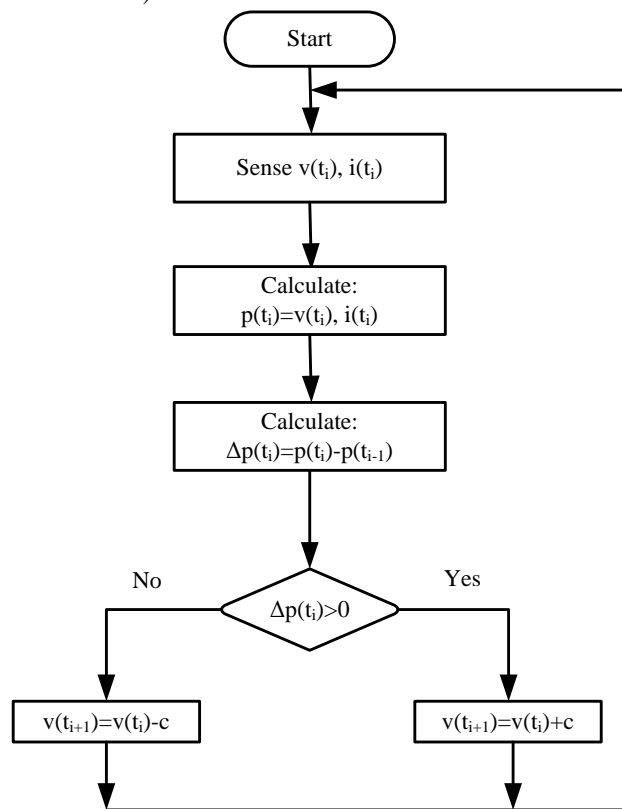


Fig. 2.7 Conventional P&O algorithm flowchart. 'c' is the step of the perturbation.

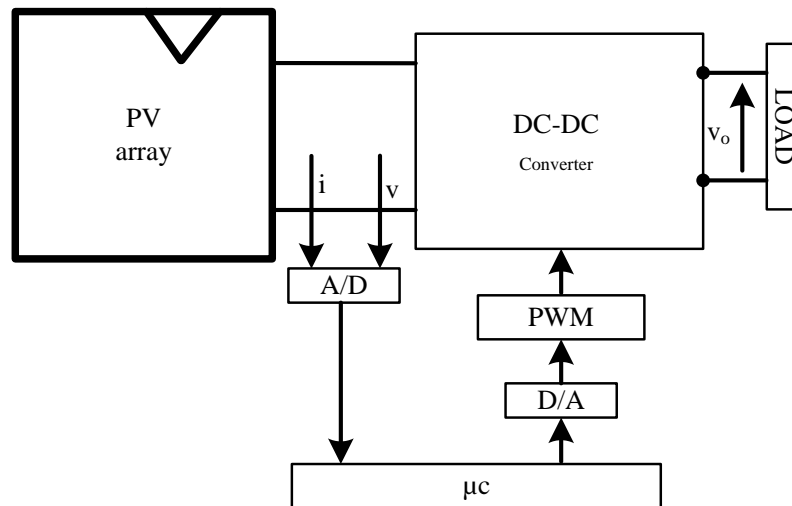


Fig. 2.8 An example of the system implementation of the P&O.

If Δp is positive, the perturbation of the operating voltage should be in the same direction of the increment. If it is negative, the system operating point obtained moves away from the MPP and the operating voltage should be in the opposite direction of the increment.

At steady state, the operating point oscillates around the MPP giving rise to the waste of some amount of available energy. The P&O algorithm can be confused during rapidly changing atmospheric conditions; e.g. Fig 2.9. To limit the negative effects associated to the above drawbacks, the P&O MPPT parameters must be customized [8] to the dynamic behavior of the specific converter adopted. Two parameters require to be optimized: the sample period of the MPPT τ_s , and the amplitude of the duty cycle perturbation Δd .

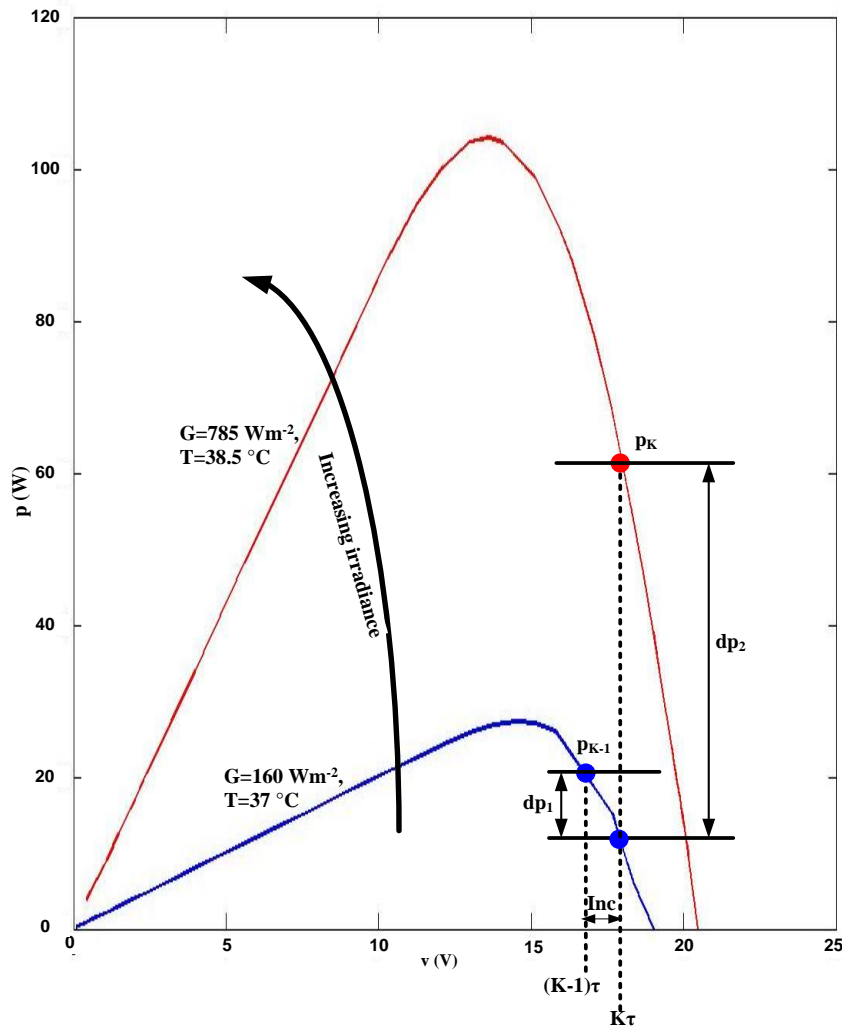


Fig. 2.9 An example of a sudden increase of irradiance; at the $k\tau$ instant $\Delta p/\Delta v$ results > 0 ; the control order to increase the operating voltage which deviate from the right MPP in the new output characteristic ($G=785 \text{ W/m}^2$).

2.3.2.2 Incremental conductance method

This method is an alternative of the P&O and was proposed in [52]. It is based on differentiating the PV power p with respect to voltage and setting the result to zero as shown in the next equation:

$$\frac{dp}{dv} = \frac{d(vi)}{dv} = i + v \frac{di}{dv} = 0 \quad (2.16)$$

From equation (2.16), the logic of this method is derived as shown in equation 2.17:

$$-\frac{i}{v} = \frac{di}{dv} \quad (2.17)$$

The left-hand side of equation (2.17) represents the opposite of the instantaneous conductance ($g=i/v$), whereas the right hand side represents its incremental

conductance. On the other hand, the incremental variations dv and di can be approximated by the increments of both parameters Δv and Δi . It is done with the aim of measuring the actual value v and i with the values measured in the previous instant. Results are shown in equation 2.18 and 2.19.

$$dv(t_2) \approx \Delta v(t_2) = v(t_2) - v(t_1) \quad (2.18)$$

$$di(t_2) \approx \Delta i(t_2) = i(t_2) - i(t_1) \quad (2.19)$$

The basic flow chart algorithm is similar of the P&O, and basically there are three conditions:

- $\Delta i/\Delta v > -i/v$; means that the operating point is at the left on the MPP and should be incremented.
- $\Delta i/\Delta v < -i/v$; means that the operating point is at the right on the MPP and should be decreased.
- $\Delta i/\Delta v \approx -i/v$; means that the operating point is at the MPP. In practice, the last condition is never satisfied due to measurement errors. For this purpose, it is usually accepted with a small error. Therefore, at the steady state, the operating point slightly oscillates around the MPP.

The advantage of the INC respect to the P&O is that it offers a good yield method under rapidly changing atmospheric conditions at the expense of the adding complex control circuit.

2.3.2.3 The only voltage photovoltaic method

Direct methods require the PV voltage and current to be measured. It is possible to find a method that only uses the PV voltage [53]. The analysis is reported for the buck converter and can be extended to the boost converter. Efficiency of the buck converter which is used as an intermediate between the solar array system and the load can be expressed as follows:

$$\eta = \frac{V_o I_o}{V^2 / R_{eq}} \quad (2.20)$$

where R_{eq} , V , V_o , I_o are the equivalent reflected resistance of the PV source, input voltage of the converter, output voltage of the converter and output current of the converter, respectively.

From equation (2.20), a different expression for the equivalent resistance of the PV source can be obtained with respect to the definition where it is expressed as a function on the electrical parameters of the PV array model:

$$R_{eq} = \frac{\eta R_L}{D^2} \quad (2.21)$$

where D is the duty cycle and R_L is the output load.

From equation (2.21), also the output power of the PV array can be expressed in a different way as shown in equation (2.22):

$$p = \frac{V^2}{R_{eq}} = \frac{(VD)^2}{\eta R_L} \quad (2.22)$$

Since the duty cycle and hence the power value is changed by a small amount between two consecutive sampling cycles, the converter efficiency (η) can be assumed to be constant over these operating conditions. For a constant resistive load, equation (2.22) is reduced to obtain the following objective function p^* :

$$p^* \propto \sqrt{p} = VD \quad (2.23)$$

The maxima of both p and its corresponding objective function p^* will coincide. p^* is maximized using the general hill-climbing technique by directly manipulating D , it tracks the maximum power closely and also responds to changes in atmospheric conditions efficiently.

Differentiating equation (2.23) respect to D , it is obtained at the MPP that the difference $D\Delta V - V\Delta D$ equals zero.

2.4 Capacitance load

Since output characteristic of SC depends on load impedance, a capacitance load was considered to be investigated for its capability to be inserted in an integration process and the time coupling between voltage and current of SC it gives access to.

2.4.1 Dynamic response

The equivalent circuit of the static model of SC where a passive impedance C is employed as a load is shown in Fig. 2.10. The characteristic equation for SC which presents a non-linear relationship between its output voltage and current is reported in

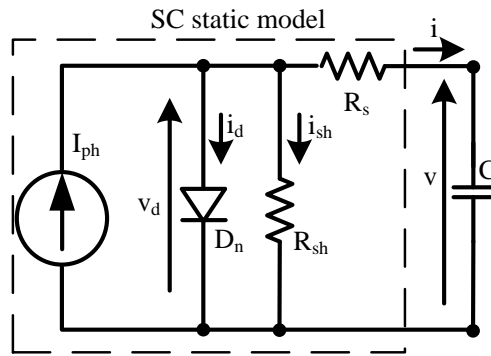


Fig. 2.10 Equivalent circuit for a capacitor c employed as a load for an SC

Chapter1 (equation (1.1)). To obtain a direct equation for the dynamic output voltage and current of SC due to c load, simplifications are performed idealizing the series and shunt resistance ($R_s \rightarrow 0$ and $R_{sh} \rightarrow \infty$). The simplified output characteristic equation is:

$$i = I_{ph} - I_0 e^{\frac{v}{nV_T}} \quad (2.24)$$

Thanks to equation (2.24), the output voltage as function of the output current is now explicit and takes the following form:

$$v = nV_T \ln\left(\frac{I_{ph} - i}{I_0}\right) \quad (2.25)$$

Due to the capacitor load C , the output voltage v can be explained dynamically as shown in equation (2.26)

$$v(t) = \frac{1}{C} \int_{t_0}^t i(t') dt' + v(t_0) \quad (2.26)$$

where t_0 and t indicate initial and instant time of the analysis, respectively; $v(t_0)$ and $v(t)$ are the output voltage corresponding at time t_0 and t , respectively; $i(t)$ is the dynamic output current.

The output voltage $v(t)$ can be replaced in equation (2.26) by its expression reported in equation (2.25); equation (2.27) is obtained:

$$nV_T \ln\left(\frac{I_{ph}-i}{I_0}\right) = \frac{1}{C} \int_{t_0}^t i(t') dt' + v(t_0) \quad (2.27)$$

The derivative of the last equation with respect to the time gives equation (2.28):

$$-\frac{I_{ph} \partial t}{C n V_T} = \frac{\partial i}{I_{ph}-i} + \frac{\partial i}{i} \quad (2.28)$$

Integrating equation (2.28) between $[t_0, t]$, the dynamic output current is obtained as reported in equation (2.29):

$$i(t) = I_{ph} \frac{1}{1 + A \exp\left(-\frac{t-t_0}{\tau_{SC}}\right)} \quad (2.29)$$

where A is equal to $(I_{ph}-i(t_0))/i(t_0)$ and τ_{SC} the time constant of the SC and is equal to $(C n \cdot V_T / I_{ph})$.

Through equation (2.26) and (2.29), the output dynamic voltage is deduced as reported in equation (2.30)

$$v(t) = -V_T \ln\left(1 + A^{-1} \exp\left(-\frac{t-t_0}{\tau_{SC}}\right)\right) + V_T \ln(1 + A^{-1}) + v(t_0) \quad (2.30)$$

The simplified model of the SC with the capacitor load was built in Matlab environment; the analytical and numerical output voltage and current are compared dynamically (Fig. 2.11(a)) and statically (Fig. 2.11(b)). As can be shown from Fig. 2.11, the simulated data reproduce the exponential and logarithm trend of the dynamic current and voltage. The values of the specific parameters for this example are reported in Table 2.2.

Table 2.2: Specific parameters of the example reported in Fig. 2.11

I_{ph} (A)	1.5
I_0 (A)	$1 \cdot 10^{-7}$
n	1.2
R_s (Ω)	0
R_{sh} (Ω)	∞
T ($^{\circ}C$)	25
C (mF)	2
τ_{SC} (μs)	0.411
$v(t_0)$ (V)	0
$i(t_0)$ (A)	$I_{sc} = I_{ph} - I_0$
A	$6.6667 \cdot 10^{-8}$

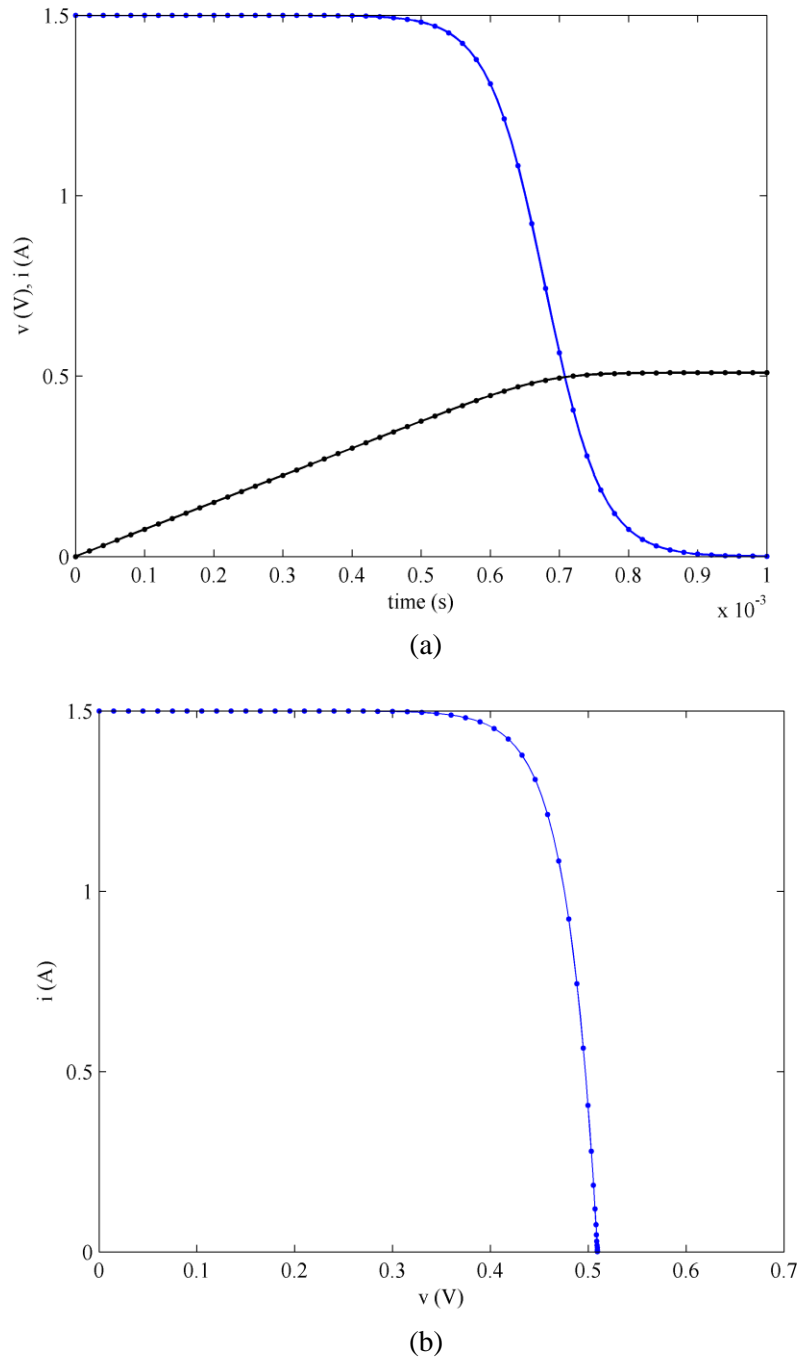


Fig. 2.11 (a) The analytical dynamic output voltage and current compared with the numerical data (b) the analytical i - v curve compared with the numerical one; line corresponds to the analytic expression while marker dot corresponds to the simulation results.

2.5 Bridge capacitor

The dynamic response of the SC due to a capacitor load has led to a novel technique to extract the maximum power available from photovoltaic structure using a single voltage sensor. The simulation is elaborated for four solar cells connected in series and can be deduced or applied for any PV structure.

2.5.1 MPP detection

Referring to the circuit reported in Fig. 2.10, power detection relies on the following relation:

$$\frac{\partial p}{\partial t} = C \left(i \frac{\partial v}{\partial t} + v \frac{\partial i}{\partial t} \right) \quad (2.31)$$

As through capacitance C the time coupling between current and voltage is available:

$$i = C \frac{\partial v}{\partial t} \quad (2.32)$$

Using equations (2.31) and (2.32) the following relationship is carried out:

$$F = \frac{\partial p}{\partial t} = C \left(\left(\frac{\partial v}{\partial t} \right)^2 + v \frac{\partial^2 v}{\partial t^2} \right) \quad (2.33)$$

The sign of the function F equal to $(\partial p / \partial t) / C$ is enough to get information on the location of the MPP using only the knowledge of the output voltage and its first and second order derivatives. When the derivative of p is zero and consequently F is zero, the working voltage point is at MPP. When F is negative (positive) the operating point is at the left on MPP (on the right). An example is shown in Fig. 2.12.

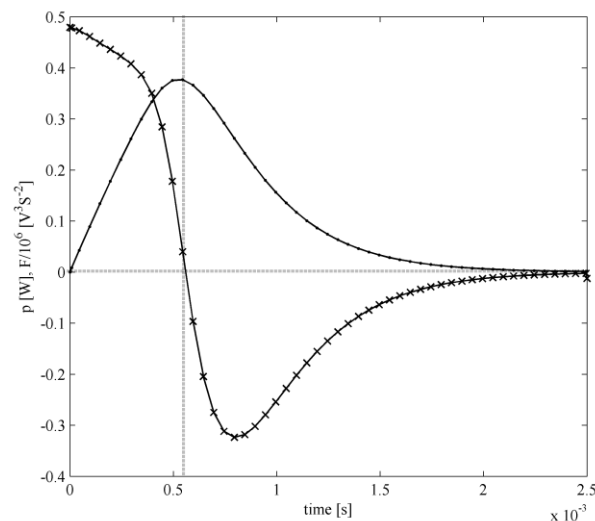


Fig. 2.12 Example of the function F ; when the value of F is zero the operating voltage is @ the MPP.

Placing a capacitive load to the SC, the output voltage increases logarithmically from the initial voltage of the capacitor to the open circuit voltage (V_{oc}) passing by the MPP. The MPP can be identified with only the knowledge of the output voltage exploiting the sign of the function F . It is only valid for capacitance load. To allow the power to be transferred to the load, a structure has to be implemented that allows two working states for the capacitor: ‘charging’ and ‘loading’ states. During ‘charging’ state, capacitor C is disconnected from the load and F is valid. During ‘loading’ state, capacitor C is disconnected from PV source and can be connected to the load for partial discharge. To allow continuous operation, a bridge capacitor topology, reported in Fig. 2.13, is implemented with two capacitors C_1 and C_2 which work in a complementary way. The output voltage control is obtained by equaling, in the mean sense, the injected current in the capacitor during ‘charge’ state with the capacitor current extracted during the load state. The basic operation of the circuit of Fig. 2.13 can be explained in the following:

- 1) The first two switches S_1 and S_2 (Fig. 2.13) work in a complementary way at a constant frequency (normally several kHz) and permit to charge C_1 and C_2 from the initial voltage to the open circuit voltage when the control unit is inactive. An example is shown in Fig. 2.14.
- 2) The control unit has the function to calculate F and consequently to command S_3 and S_4 with the following logic (1 and 0 note that the switch is on and off, respectively):

$$S_3 = \begin{cases} 1; (F \leq 0) \& (S_1 = 0; S_2 = 1) \\ 0; \text{else} \end{cases}$$

$$S_4 = \begin{cases} 1; (F \leq 0) \& (S_1 = 1; S_2 = 0) \\ 0; \text{else} \end{cases}$$

The sign of F is evaluated for each switching period by activating the control unit; consequently the output voltage v (equal to the voltage v_1 of the capacitor c_1 when S_1 is on and equals to the voltage v_2 of the capacitor c_2 when S_2 is on) reach the MPP and works around it. When the output voltage exceeds the MPP (F becomes negative), the voltage control requires the capacitor to partial discharge on the load (through S_3 if S_1 is off or through S_4 if S_2 is off). This operation reports the operating voltage slightly lower than MPP with a constant time τ equal to $z c_1$ or $z c_2$, where z is the load impedance. The operation is repeated and the output voltage working point remains around MPP. An example is reported in Fig. 2.15.

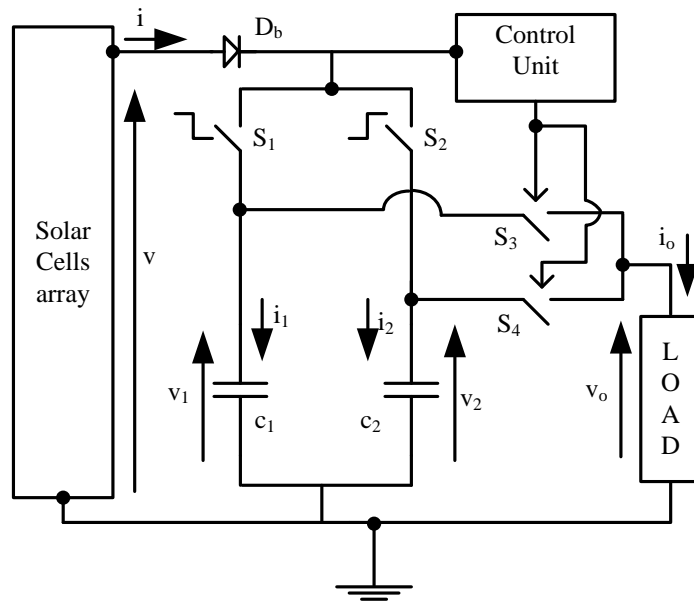


Fig 2.13 Bridge capacitor as an interface between the solar cells array and the load; opportunity controlled to extract the maximum power from the PV source in all conditions.

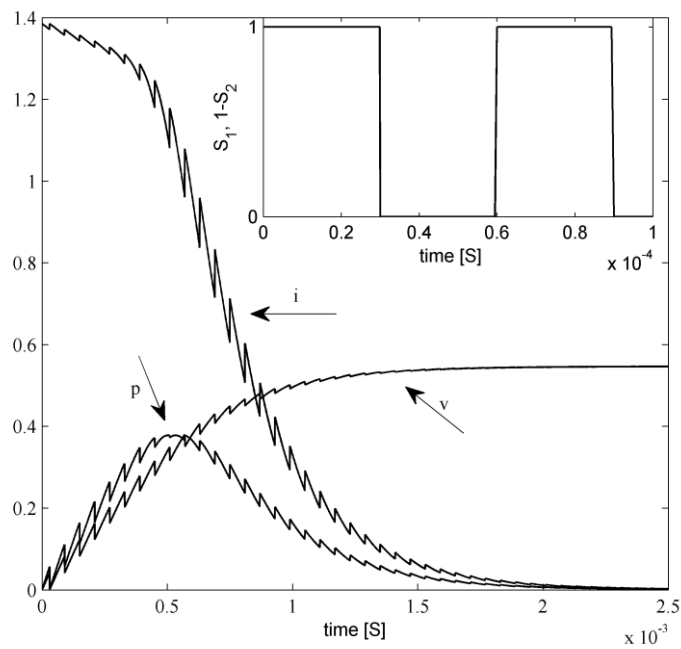


Fig. 2.14 An example of the output dynamic data voltage, current and power when the switch of the bridge operates in a complementary manner with the control unit inactivate.

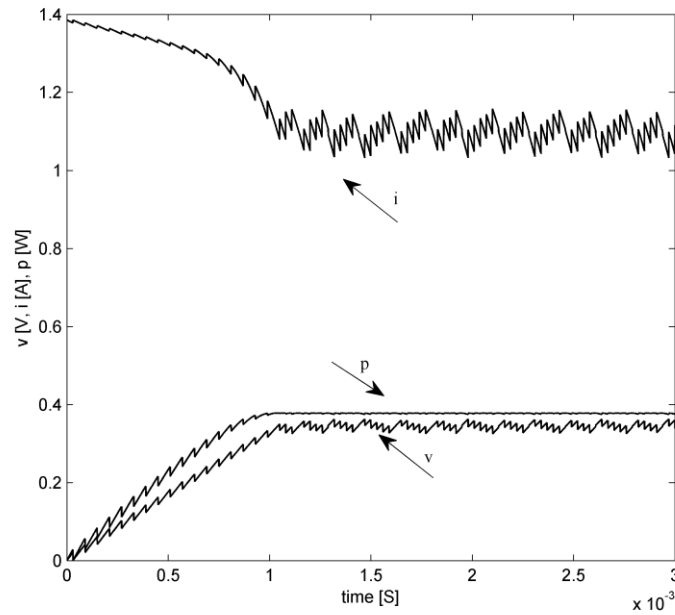
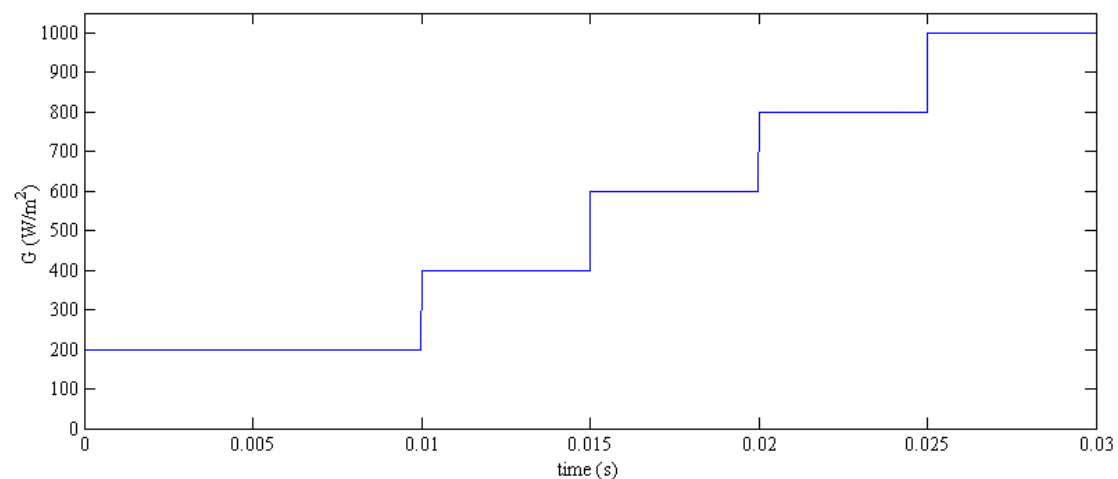


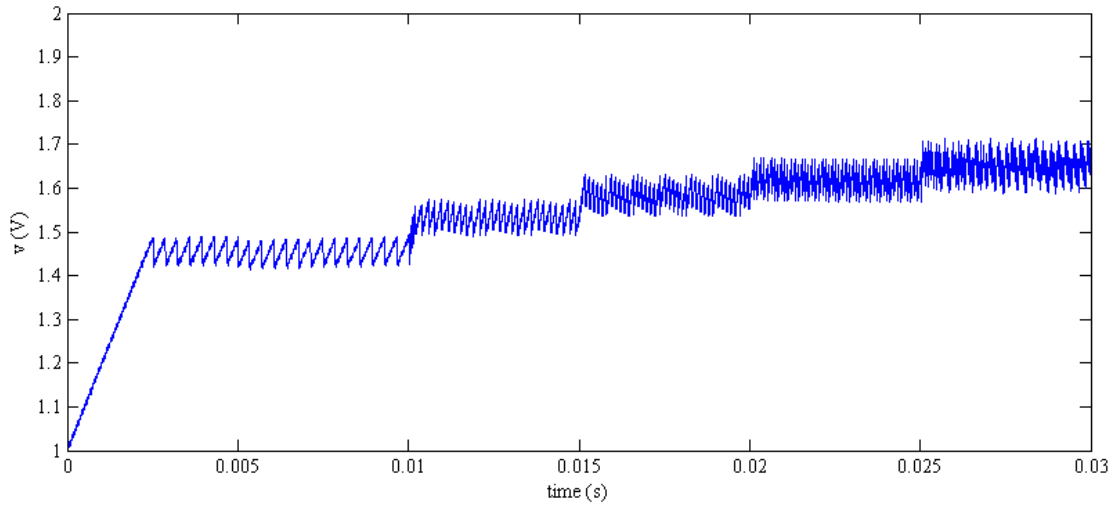
Fig. 2.15 An example of the output dynamic data voltage, current and power when the control unit is activate. It is noted that after about 1 ms the voltage working point reach the MPP and remains around it.

2.5.2 Simulation results

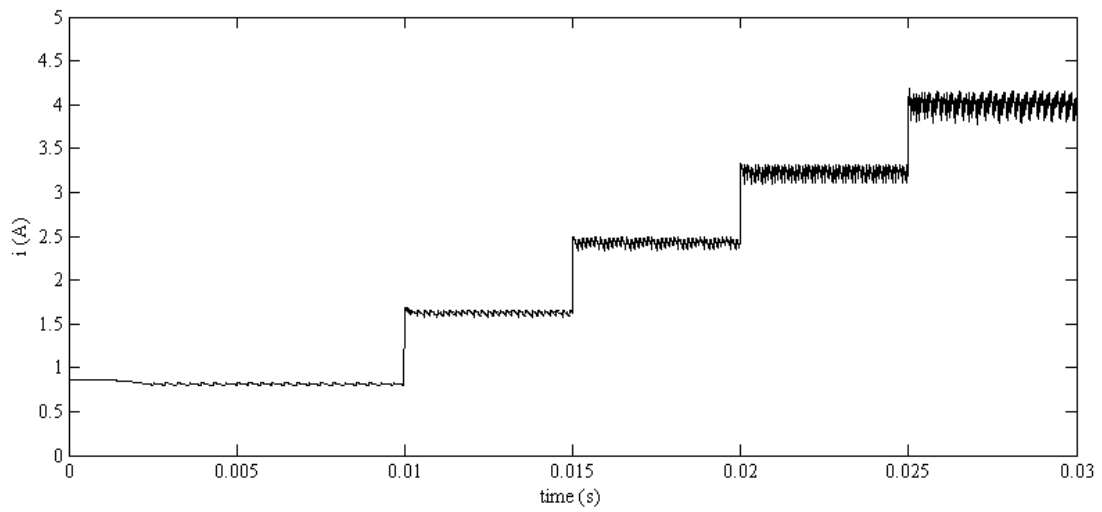
Simulation curves are reported in Fig. 2.16, where large changes of irradiance G (Fig. 2.16(a)) are introduced. As working voltage reaches the first operation point, the reaction to the new operation condition happens with the SCs constant time τ_{SC} time scale (Fig. 2.16(b) and Fig. 2.16(c) report the output voltage and output current, respectively). Fig. 2.16 (d) and (e) show the instant power generated from the PV source with the effective maximum power and a zoom for a cycle, respectively.



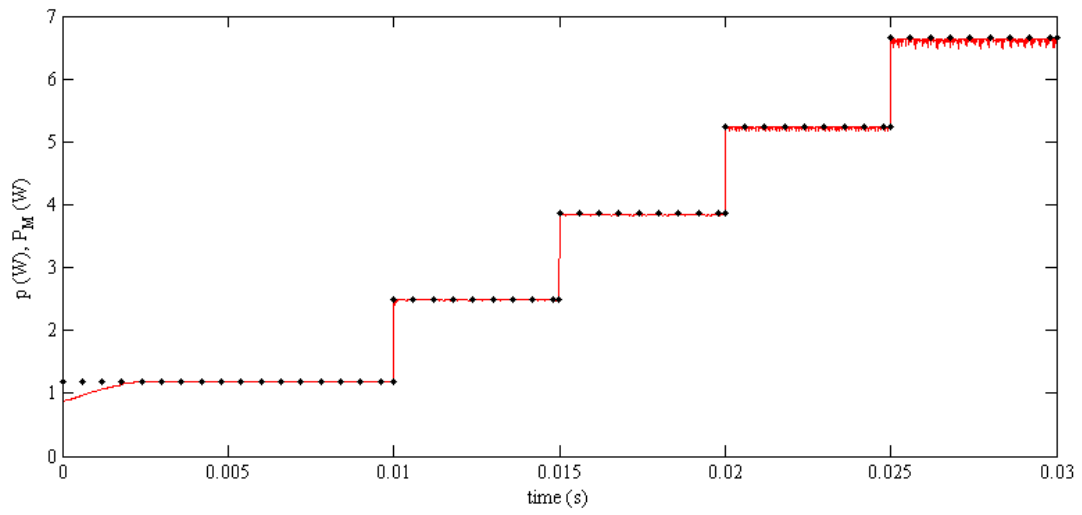
(a)



(b)



(c)



(d)

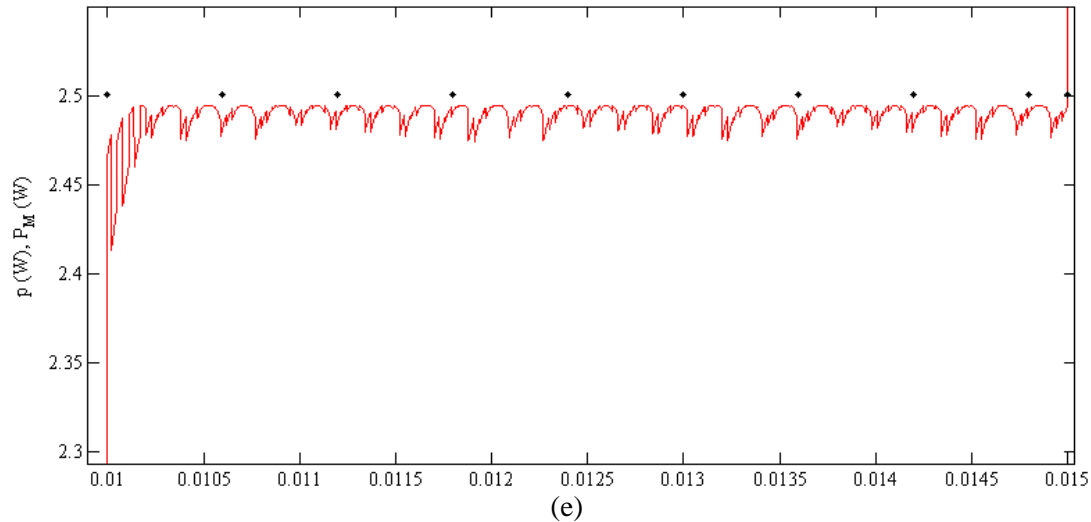


Fig. 2.16 Data output of SC arrays due to bridge capacitor topology in different irradiance conditions; (a) dynamic variation of the irradiance condition, (b) dynamic output voltage, (c) dynamic output current, (d) instant output power (solid line) with known optimum power capability (dot marker), (e) zoom of the output power during at 400 W/m^2 .

An estimation of method efficiency, defined in equation (2.34), is performed.

$$\eta = \frac{\int_{t_0}^t p(t') dt'}{\int_{t_0}^t P_M(t') dt'} \quad (2.34)$$

where $p(t')$ is the actual power produced by the PV generator under the control of the MPPT and P_M is the true maximum power that the array could produce under the given temperature and irradiance. (Since temperature and irradiance are both functions of time, $p(t')$ and P_M are also time varying). The results obtained for five irradiance conditions (Fig. 2.16 (a)) and at fixed temperature (30°C) are reported in Table 2.3.

Table 2.3: The calculated efficiency for five distinct conditions

$G \text{ W/m}^2$	η
200	0.993
400	0.995
600	0.994
800	0.995
1000	0.995

2.5.3 Experimental results and considerations

A real system is built as a prototype in the Power Electronics Lab to show the MPPT behavior and it is based on six monocrystalline SCs series connected (characterized in Chapter 1) which feed the bridge capacitor MPPT converter. An example is reported

in Fig. 2.17 and shows the output voltage of the array of SC oscillating around the estimated MPP. The measurement was done inside laboratory with irradiance equals to $300 \text{ W/m}^2 \pm 10$; the average working temperature results to $62 \text{ }^\circ\text{C} \pm 2$; the switch frequency of S_1 and S_2 equals to 10 kHz and a resistive load of $1 \text{ } \Omega \pm 0.1$. The estimation of the optimum working voltage is done using the open-circuit voltage method and results to be 2.08 V ($0.75 \cdot V_{oc}$).

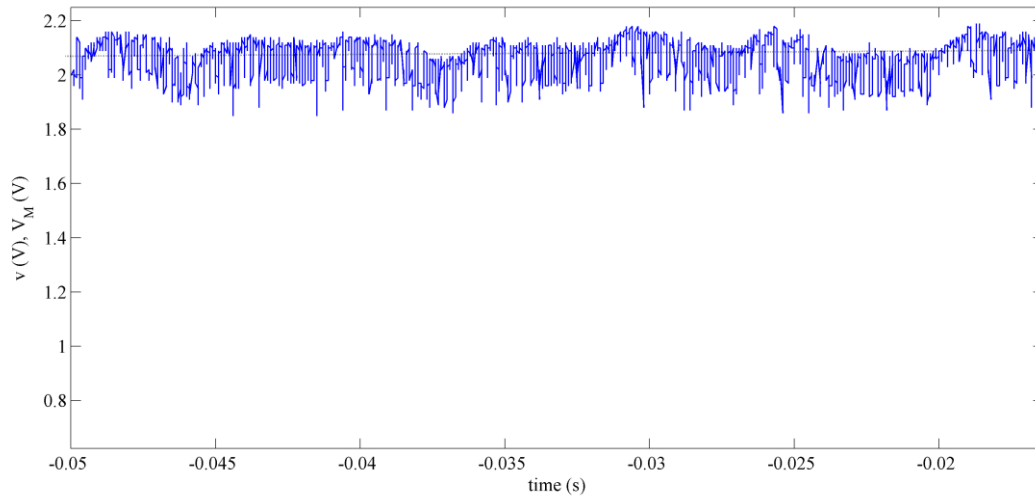


Fig.2.17 The estimated MPP and the output operating voltage v of six SCs series connected and interfaced through a bridge capacitor MPPT converter.

This novel topology collects the main advantages of the MPPT methods presented in literature and can be reassumed as follows:

- it is simple to be implemented;
- it is based on a single voltage sensor [53];
- no prior knowledge of the PV parameters is needed in contrast with the indirect methods [40-47];
- high convergence velocity to MPP [47];
- possibility of integration of the interface system (inducterless);
- insensitive to rapidly changing atmospheric conditions [8];
- keeps efficiency higher than 99 % in all the operation conditions for a specific load (simulation results)

2.6 Conclusion

MMPT algorithms benefits in PV system are discussed. An analysis of the use of the DC-DC converter for a specific application is reported. A review of the MPPT algorithms is done subdividing the approaches in 'indirect' and 'direct' methods. Some representative methods are discussed. The behavior of an SC system with a capacitive load is analyzed and a characteristic time t_{SC} defined. A novel single sensor, extremely fast converging bridge capacitor MPPT algorithm is proposed.

The bridge capacitor topology is analyzed, simulated with Matlab model and a prototype realized. This topology presents a novel approach to MPPT and is suitable for application with inductorless converters. At present, it has to be dimensioned for a given application or a specific load.

CONCLUSION

In this thesis, a photovoltaic power systems is presented. Parameters evaluation of the most exploitable static model of solar cells are investigated using two distinct methods 'N-R' and 'SVO'. It is shown that SVO method deliver a fast, stable result suitable for commercial application in solar cell in-line testing and characterization and solar panel testing as indicated in International Standard CEI EN 61215 and CEI EN 61646.

The effects of the parasitic capacitance of solar cells are evidenced and justified analytically underlying a dynamic model. It affect flash test and fast techniques and treat the stability and reliability of the maximum power point techniques when high frequency switching (several kHz) converters are used.

A review of the maximum power point tracking (MPPT) algorithms for photovoltaic systems is reported. The dynamic effects of SC response to a capacitive load are analyzed. A novel technique derived from this consideration is proposed which collects the main advantages of the most used algorithms.

BIBLIOGRAPHY

- [1] http://www.keithley.com/solar_cell (March 2010)
- [2] <http://www.ni.com/pytesting> (March 2010)
- [3] <http://www.solarmagic.com> (June 2009)
- [4] <http://www.st.com/stonline/stappl/cms/press/news/year2010/p3031.htm> (July 2010)
- [5] A.Luque, S. Hegedus, “Handbook of Photovoltaic Science and Engineering,” Wiley, England, 2003.
- [6] L. Castaner, S. Silvestre, “Modelling Photovoltaic Systems Using Pspice,” Wiley, 2002.
- [7] W. M. Keogh, A.W. Blakers, A. Cuevas, “Constant voltage I-V curve flash tester for solar cells,” Solar Energy Materials & Solar Cells, Vol 81, pp. 183–196, 2004
- [8] N. Femia, G. Petrone, G. Spagnuolo, B, and M. Vitelli, “Optimization of perturb and observe maximum power point tracking method,” IEEE Transactions on Power Electronics, Vol. 20, pp. 963–973, July 2005.
- [9] H.Tian, L. Liu, B. Liu, S.Yuan, X. Wang, Y. Wang, T. Yu, Z. Zou, “Influence of capacitance characteristic on dye-sensitized solar cell’s IPCE measurement,” Journal of Physics, Vol. 42, 045109, 2009.

- [10] J. A. Gow, C.D. Manning, "Development of a photovoltaic array model for use in power electronics simulation studies," IEE Proceedings of Electric Power Applications 146 (1999), 193–200.
- [11] E.E. van Dyk, E.L. Meyer, "Analysis of the effect of parasitic resistances on the performance of photovoltaic modules," Renewable Energy 29 (2004) 333-344.
- [12] M.A. Vitorino, L.V. Hartmann, A.M.N. Lima, M.B.R. Correa, "Using the model of the solar cell for determining the maximum power point of photovoltaic systems," 12th European Conference on Power Electronics and Applications (2007) 1-10.
- [13] M. Zagrouba, A. Sellami, M. Bouaïcha, M. Ksouri, "Identification of PV solar cells and modules parameters using the genetic algorithms," Solar Energy 84 (2010), 860-866.
- [14] M. Wolf, H. Rauschenbach, "Series resistance effects on solar cell measurements," Advanced Energy Conversion 3 (1963), 455-479.
- [15] S.K. Agrawal, R. Muralidharam, A. Agrawala, V.K. Tewary, S.C. Jain, "A new method for the measurement of series resistance of solar cells," Journal Physics D: Applied Physics 14 (1981) 1115-1124.
- [16] J. Cabestany, L. Castaner, "A simple solar cell series resistance measurement method," Revue de Physique Appliquée 18 (1983), 565-567.
- [17] M. Warashina, A. Ushirokawa, "Simple method for the determination of series resistance and maximum power of solar cell," Japanese Journal of Applied Physics 19 (1980), 179-182.
- [18] A. Kaminski, J.J. Marchand, A. Laugier, "I–V methods to extract junction parameters with special emphasis on low series resistance," Solid-State Electronics 43 (1999) 741 745.
- [19] E. Radziemska, "Dark I–U–T measurements of single crystalline silicon solar cells," Energy Conversion and Management 46 (2005), 1485-1494.
- [20] K. Rajkanan, J. Shewchun, "A better approach to the evaluation of the series resistance of solar cells," Solid-State Electronics 22 (1979), 193-197.

- [21] A.G. Aberle, S.R. Wenham, M.A. Green, A New Method for Accurate Measurement of the Lumped Series Resistance of Solar Cells, 23th IEEE Photovoltaic Specialists Conference (1993), 133-139.
- [22] T. Easwarakhanthan, J. Bottin, I. Bouhouch, C. Boutrit, "Nonlinear Minimization Algorithm for Determining the Solar Cell Parameters with Microcomputers," International Journal of Sustainable Energy 4 (1986), 1-12.
- [23] R.J. Bennet, Interpretation of Forward bias behavior of Schottky barriers, "IEEE Transactions on Electron Devices 34 (1987)," 935-937.
- [24] M. Haouari-Merbah, M. Belhamel, I. Tobias, "J.M. Ruiz, Extraction and analysis of solar cell parameters from the illuminated current–voltage curve," Solar Energy Materials and Solar Cells 87 (2005), 225 233.
- [25] J. A Jervase, H. Bourdouden, and A. Al-Lawati, " Solar cell parameter extraction using genetic algorithms," Measurement Science and Technology 12, (2001), 1922-1926.
- [26] M. Ye, X. Wang, and Y. Xu, "Parameter extraction of solar cells using particle swarm optimization", Journal of Applied Physics 104, (2009), 0945021–0945028.
- [27] E. Dallago, D. Finarelli, P. Merhej, "Evaluation and analysis of single and dual diode solar cell model parameters,"
- [28] E. Dallago, D. Finarelli, P. Merhej, "Method based on single variable to evaluate all parameters of solar cells," Electronic Letters (46), (2010),
- [29] P. Merhej, E.Dallago, D. Finarelli, "Effect of capacitance on the output characteristics of Solar Cells," Prime, (2010)
- [30] K. Bouzidi, M. Chegaar, A. Bouhemadou, "Solar cells parameters evaluation considering the series and shunt resistance," Solar Energy Materials & Solar Cells 91, (2007), 1647–1651.

- [31] J. A. Gow, C.D. Manning, "Development of a photovoltaic array model for use in power electronics simulation studies," IEE Proceedings of Electric Power Applications 146 (1999), 193–200.
- [32] F. Khan, S.N. Singh, M. Hussain, "Effect of illumination intensity on cell parameters of a silicon solar cell," Solar Energy Materials & Solar Cells, (2010), article in press.
- [33] M. C. Alonso-García, J. M. Ruiz, F. Chenlo, "Experimental study of mismatch and shading effects in the I - V characteristic of a photovoltaic module," Solar Energy Materials & Solar Cells (2006), 329-340
- [34] N. D. Kaushika, A. K. Rai, "An investigation of mismatch losses in solar photovoltaic cell networks," Energy (2007), 755-759
- [35] S. Silvestre, A. Boronat, A. Chouder, "Study of bypass diodes configuration on PV modules," Applied Energy (2009), 1632-1640
- [36] V. Salas, E. Olias, A. Barrado, A. Lazaro, "Review of the maximum power point tracking algorithms for stand-alone photovoltaic systems," Solar Energy Materials & Solar Cells 90, 2006, 1555–1578.
- [37] T. ESRAM, and P. L. Chapman, "Comparison of photovoltaic array maximum power point tracking techniques," IEEE Transactions on Energy Conversion 22, (2007), 439-449.
- [38] J.M. Enrique, E. Duran, M. S. De-Cardona b,1, J. M. Andujar, "a Theoretical assessment of the maximum power point tracking efficiency of photovoltaic facilities with different converter topologies," Solar Energy 81, (2007), 31–38
- [39] M. Veerachary, "Analysis of photovoltaic maximum power point trackers," IEEE Transactions on Industry 127, (2007), 1215-1223
- [40] Tamer T. N. Khatib, A. Mohamed, N. Amim, K. Sopian, "An improved indirect maximum power point tracking method for standalone photovoltaic systems," World Scientific and Engineering Academy and Society (2010), 56-62
- [41] N. Takehara, S. Kurokami, "Power control apparatus and method and power generating system using them", Patent US5,654,883 (1997).

- [42] H. E.-S. A. Ibrahim, et al., "Microcomputer controlled buck regulator for maximum power point tracker for DC pumping system operates from photovoltaic system," *Fuzzy Systems Conference Proceedings* (1999), 406–411.
- [43] J. J. Schoeman, J. D. van Wyk, "A simplified maximal power controller for terrestrial photovoltaic panel arrays," *IEEE Power Electronics Specialists Conference* (1982), 361–367.
- [44] P. Chetty, "Maximum power transfer system for a solar cell array," US4,604,567, (1986).
- [45] D. Lafferty, "Regulating control circuit for photovoltaic source employing switches energy storage and pulse width modulation controller," Patent US5,270,636, (1993).
- [46] T. Noguchi, et al., "Short-current pulse-based adaptive maximum power point tracking for a photovoltaic power generation system," *Elect. Eng. Japan* 139 (2002), 65–72.
- [47] M. A. Vitorino, L. V. Hartmann, A. M. N. Lima, M. B. R. Correa, "Using the model of the solar cell for determining the maximum power point of photovoltaic systems," *12th European Conference on Power Electronics and Applications* (2007), 1-10.
- [48] Z. Salameh, D. Taylor, "Step-up maximum power point tracker for photovoltaic arrays," *Solar Energy* 44 (1990), 57–61.
- [49] W. J. A. Teulings, J. C. Marpinard, A. Capel, "A maximum power point tracker for a regulated power bus," *Proceedings of the European Space Conference*, 1993.
- [50] Y. Kim, H. Jo, D. Kim, "A new peak power tracker for cost-effective photovoltaic power systems," *IEEE Proc. Energy Conversion Eng. Conf. IECEC* (1996), 1673–1678.
- [51] Ch. Hua, J. Lin, Ch. Shen, "Implementation of a DSP-controlled PV system with peak power tracking," *IEEE Trans. Ind. Electron.* 45 (1998), 99–107.

[52] K.H. Hussein, I. Muta, T. Hoshino, M. Osakada, "Maximum photovoltaic power tracking: an algorithm for rapidly changing atmospheric conditions," IEE Proc. Generation Transmission Distrib. 142 (1995), 59–64.

[53] N. Dasgupta, A. Pandey, A. K. Mukerjee, "Voltage-sensing-based photovoltaic MPPT with improved tracking and drift avoidance capabilities," Solar Energy Materials & Solar Cells (2008), 1552-1558.